Wind Distribution in the Eye of Tropical Cyclone Revealed by a Novel Atmospheric Motion Vector Derivation

Taiga Tsukada[1,2] , Takeshi Horinouchi[1,3] , and Satoki Tsujino[4]

[1]Faculty of Environmental Earth Science, Hokkaido University, Sapporo, Japan, [2]Now at Cooperative Institute for Research in the Atmosphere, Colorado State University, Fort Collins, CO, USA, [3]Typhoon Science and Technology Research Center, Yokohama National University, Yokohama, Japan, [4]Department of Typhoon and Severe Weather Research, Meteorological Research Institute, Ibaraki, Japan

Abstract Observations of wind distribution in the eye of tropical cyclones (TCs) are still limited. In this study, a method to derive atmospheric motion vectors (AMVs) for TCs is developed, where selection from multiple local rotation speeds is made by considering continuity among neighboring grid points. The method is applied to 2.5-min interval image sequences of three TCs, Lan (2017), Haishen (2020), and Nanmadol (2022), observed by the *Himawari-8* satellite. The results are compared with AMVs derived from research-based 30-s *Himawari-8* special observations conducted for Haishen and Nanmadol, as well as with in-situ dropsonde observations conducted for Lan and Nanmadol. In these storms, the AMVs obtained from the 2.5-min interval images in the eye are found to be in good agreement with the dropsonde observations. Examinations of AMVs in the eye reveal transient azimuthal wavenumber-1 features in all three TCs. These features are consistent with algebraically growing wavenumber-1 disturbances, which transport angular momentum inward and accelerate the eye rotation. In the case of Lan, the angular velocity in the eye increased by approximately 1.5 times within 1 hr. This short-term increase is further examined. Visualization of low-level vorticity in the eye and angular momentum budget analysis suggest that angular momentum transport associated with mesovortices played an important role in the increase of tangential wind and the homogenization of angular velocity in the eye of Lan.

Plain Language Summary Observations of winds in the eye of tropical cyclones (TCs) are still limited. In this study, a new method is developed to derive the winds by objectively tracking the clouds in the eye of TCs using geostationary meteorological satellite imagery. The method is applied to 2.5-min interval image sequences of three TCs observed by the *Himawari-8* satellite. The estimated winds in the eye are found to be in good agreement with in-situ dropsonde observations. Examinations of asymmetric motions in the eye reveal transient azimuthal wavenumber-1 features in all three TCs. These features contribute to the inward transport of angular momentum and acceleration of eye rotation. In the eye of Typhoon Lan (2017), the rotation speed increased by about 1.5 times within an hour. The study further examines this short-term acceleration and suggests that angular momentum transport associated with mesoscale vortices played an important role in the measured increase in rotation speed and the homogenization of the rotation in the eye.

1. Introduction

Studies on the dynamics in the eye of tropical cyclones (TCs; also see Table 1 for this and all other acronyms) have primarily relied on theoretical and numerical frameworks (e.g., Hendricks et al., 2009; Nolan & Montgomery, 2000; Rozoff et al., 2009; Schubert et al., 1999; Yau et al., 2004). Particularly, the impact of asymmetric motions on the inner-core structure has been the subject of many of these studies. These investigations have highlighted the significance of exponentially growing barotropic instability and algebraically growing wavenumber-1 disturbances as described below.

The exponentially growing barotropic instability, as demonstrated in the theoretical study by Schubert et al. (1999), is recognized as a fundamental mechanism for inner-core dynamics through idealized unforced numerical simulations (e.g., Hendricks et al., 2009; Hendricks & Schubert, 2010; Kossin & Schubert, 2001), forced simulations (e.g., Hendricks et al., 2014; Rozoff et al., 2009), and full-physics simulations (e.g., Nguyen et al., 2011; Yau et al., 2004). This process has been shown to contribute to formation of polygonal eyewalls (e.g., Lewis & Hawkins, 1982; Muramatsu, 1986) and eyewall mesovortices (e.g., Aberson et al., 2006; Hendricks et al., 2012; Wingo & Knupp, 2016; Wurman & Kosiba, 2018) observed in radar images. The similarities between vortical cloud swirls in the eye observed in satellite images and vorticity distribution in numerical simulations

Validation: Taiga Tsukada
Visualization: Taiga Tsukada
Writing – original draft: Taiga Tsukada
Writing – review & editing:
Taiga Tsukada, Takeshi Horinouchi,
Satoki Tsujino

Table 1
A List of Acronyms

Acronym	Definition
AMV	Atmospheric motion vector
DS	Dropsonde
GMS	Geostationary meteorological satellite
H23	Horinouchi et al. (2023)
IBTrACS	International Best Track Archive for Climate Stewardship
JMA	Japan Meteorological Agency
JTWC	Joint Typhoon Warning Center
KE01	Kossin and Eastin (2001)
MAD	Mean-absolute difference
MAE	Mean-absolute error
PV	Potential vorticity
RMSD	Root-mean-square difference
RMSE	Root-mean-square error
RMΩ	Radius of maximum angular velocity
RMW	Radius of maximum wind
SAR	Synthetic aperture radar
T-PARCII	Tropical cyclones-Pacific Asian Research Campaign for Improvement of Intensity estimations/forecasts
TC	Tropical cyclone
TH20	Tsukada and Horinouchi (2020)

were also highlighted (Kossin et al., 2002; Kossin & Schubert, 2004). Using aircraft flight-level data, Kossin and Eastin (2001; hereinafter, KE01) reported the short-term (within 1 hr) increases in angular velocity in the eyes of a number of TCs. They referred to the period before the increase, characterized by a peak in angular velocity near the eyewall, as "regime 1." The phase after the increase, where the maximum angular velocity is observed near the storm center, was labeled as "regime 2." The transition from regime 1 to regime 2 was marked by a relaxation of flow across the eye and eyewall toward a rigid body rotation, which caused an increase in local tangential flow and angular momentum in the eye. They explained the cause of the regime transition as the mesovortices, formed from the breakdown of the eyewall vorticity ring due to barotropic instability, transporting angular momentum inward and expelling the relatively weaker vorticity in the eye.

Another asymmetric motion related to the algebraically growing wavenumber-1 disturbance in the eye was proposed by Nolan and Montgomery (2000) who applied a theory by Smith and Rosenbluth (1990) for plasma to TCs. This theory demonstrates that an axi-symmetric barotropic vortex with a peak in rotational angular velocity at a non-zero radius, that is, having the radius of maximum angular velocity (RMΩ), can exhibit a wavenumber-1 disturbance whose energy grows linearly with time over a sufficiently long period. This "algebraically growing" wavenumber-1 disturbance exists even when no exponentially growing unstable mode exists. However, its dynamical role has not received much attention until recently. As an observational study, Marks et al. (2008) analyzed aircraft observational data in Hurricane Hugo (1989) and reported that the locations of the flight-level minimum pressure and minimum wind speed in the eye, which were carefully deduced, rotated counterclockwise at a period of around 19 min, approximately the same as the rotational period at the RMΩ locating inside the radius of maximum wind (RMW). The characteristics of this phenomenon are suggested to be consistent with the algebraically growing wavenumber-1 disturbances. While this mechanism has been recognized in terms of vortex Rossby waves (Guinn & Schubert, 1993; Montgomery & Kallenbach, 1997) and the trochoidal motion of the storm, Horinouchi et al. (2023; hereinafter, H23) recently proposed its potential importance for the redistribution of angular momentum based on satellite observations as described later.

Observational research on these processes is relatively limited due to the challenges of capturing the details of extreme phenomena such as TCs that form and develop over the ocean, with observing winds in the eye being particularly challenging. Although aircraft observations provide reliable data on wind distribution in the eye, it usually takes ~1 hr to horizontally cover the inner-core region, and steady-state conditions are often assumed due to the lengthy observation periods. Airborne radar also cannot observe the wind in the eye due to the lack of precipitation particles.

Some satellite-based wind observations allow for dense monitoring of instantaneous or sustained wind distribution in the eye. For example, using C-band Synthetic Aperture Radar (SAR) on low-Earth-orbit satellites, wind estimation in the eye can be achieved with a horizontal resolution of about 1 km (Mouche et al., 2017, 2019; Zhao et al., 2018). Dense wind observations also enable estimation of horizontal distributions of vorticity and convergence/divergence. Unfortunately, C-band SAR observations are limited to twice daily viewing, and their operational availability is limited.

Geostationary meteorological satellites (GMSs) provide uninterrupted observations of TCs throughout their lifecycle. If atmospheric motion vectors (AMVs; see Menzel, 2001, and the references therein) could be calculated using consecutive images, it allows us to estimate dense wind distribution in the eye. However, with conventional second-generation GMSs, which have a typical observation frequency of ~30 min except for some super-rapid-scan operations (Hasler et al., 1998), it was not possible to estimate wind distribution in the inner-core region of TCs due to their long-time intervals, especially in areas with high wind speeds and rotations.

In recent years, third-generation GMSs such as the *Himawari-8*, which began operating in 2015, have significantly improved the spatiotemporal and wavelength resolution compared to their predecessors (Bessho et al., 2016; Schmit et al., 2017). For instance, the *Himawari-8/9* and the *GOES-16/17/18* have twice the spatial resolution of their predecessors, with 0.5 km for a visible channel and 2 km for infrared channels at nadir. In particular, the rapid-scan observations for TCs are made every 2.5 min in the target area of *Himawari-8/9* and every 1 min in the meso sector of the *GOES-16/17/18*, both covering an area of ~1,000 km × 1,000 km. To the best of the authors' knowledge, Horinouchi et al. (2020) is the first to effectively utilize high-frequency target-area observations from third-generation GMSs to study TC inner-core dynamics. The mentioned improvements greatly enhance the ability to calculate AMVs around TCs. However, their current application is limited to studying winds near the tropopause or outer regions away from the eye (Dai et al., 2019; Dunion et al., 2002; Dunion & Velden, 2002; Elsberry et al., 2023; Fukuda et al., 2020; Molinari & Vollaro, 1989; Oyama, 2017; Oyama et al., 2016; Ryglicki et al., 2021; Sears & Velden, 2012; Stettner et al., 2019; Velden et al., 1998; Velden & Sears, 2014). This limitation would be due to the difficulty of estimating winds in the eye, even with the improved observation frequency provided by third-generation GMSs.

In a recent study, H23 investigated low-level AMVs obtained in the eye of Typhoon Haishen (2020) using research-based special observations with the *Himawari-8*, which were conducted every 30 s. They identified both stationary and transient asymmetric features in the eye that were associated with an algebraically growing wavenumber-1 disturbance. These features were found to be important in the angular momentum transport towards the storm center, which resulted in an acceleration of the rotation in the eye. They suggested that the wavenumber-1 disturbance might be one of the major processes that redistribute potential vorticity in the eye to increase rotation near the center.

H23 employed a template matching method with cross-correlation to derive AMVs. There was no special processing specifically designed for TCs, except that five consecutive images were used simultaneously, but with the short interval of 30 s, they were able to obtain sufficient AMVs. To demonstrate the effect of the high-frequency imaging, they also conducted an experiment in which the time interval was deliberately increased and showed that the number of obtained AMVs decreases as the observation frequency decreases, suggesting the need for elaborated methods to estimate the wind distribution.

When deriving AMVs in the inner-core region using a relatively long-time interval (e.g., 2.5 min) image sequence, three major obstacles emerge that are not significant in a shorter interval (e.g., 30 s) image sequence:

1. Large rotational component: the TC inner-core region has a large rotational angular velocity, making it difficult for the simple template matching algorithms that assume parallel motion of templates.
2. Cloud deformation: due to the spatial shear of the flow in the eye and eyewall (e.g., Martinez et al., 2019), clouds are deformed, resulting in a loss of shape identity of the tracking target between consecutive images.

3. Cloud generation and dissipation: cloud generation/dissipation and cloud motion can be indistinguishable, leading to incorrect estimates.

These characteristics can occur individually or simultaneously. Obstacle one is often mitigated by considering the rotation, or in general, affine transformation of templates (Wolberg, 1990). However, obstacles 2 and 3 change template images in a non-affine transformable manner, so the best match obtained by such a method does not always match the true destination of advection. Also, since obstacles 2 and 3 fundamentally degrade the cross correlation of between templates, we need to consider relatively low correlation whether or not rotation is considered. To do so would increase erroneous matches, so an effective selection method from multiple candidates would be needed. To solve these problems, we devise a method in which a selection method is incorporated by considering rotation. This selection method is similar to a median filter approach (Schultz, 1990) developed to resolve directional ambiguities in wind fields obtained from spaceborne scatterometers, and the relaxation method (Rosenfeld et al., 1976) in which similarity among the results for surrounding grid points is considered. These methods are reviewed after introducing our method in Section 3.3. Among the general obstacles in deriving AMVs, two challenges related to illumination changes and occlusions exist. In this study, these issues are partially addressed through parameter settings and quality controls developed in H23.

Tsukada and Horinouchi (2020; hereinafter, TH20) developed a method to estimate the tangential wind profile in the eye as a function of radius. The method uses spectral analysis for azimuth-time cross section of rapid-scan imagery taken by GMSs. By applying the method to a 2.5-min interval image sequence of Typhoon Lan (2017), the wind distribution in the eye was successfully estimated. The application of this method also provided observational insights into the dynamics of concentric eyewall replacement (Tsujino et al., 2021). However, the method only provides the representative tangential wind speed over a period of around 1 hr, providing no asymmetric motion. Here, the expression "representative tangential wind speed" refers to a value that is close to the average azimuth and time. Therefore, it does not contain variations on short time scales or asymmetric motions introduced above. As a result, TH20 separately conducted a subjective analysis of asymmetric motions in the eye, and they found some mesovortices and striations in the eye of Lan.

It is desirable to investigate the wind distribution in the inner-core region of numerous TCs and accumulate observational evidence by obtaining AMVs not only from 30-s observations but also from operational 1-min or 2.5-min rapid-scan observations. Therefore, this study is aimed at developing a two-dimensional cloud tracking method for TCs by extending the method of H23 by considering the characteristics of TCs. Furthermore, we investigate the TC dynamics based on the AMVs obtained from the method.

Section 2 provides a review of the cloud tracking method developed by H23. In Section 3, the data used in this study and the developed TC-specific cloud tracking method are documented. In Section 4, the results of applying the developed method to three intense TCs and evaluation of their uncertainties are provided. In Section 5, the asymmetric motions in the eye are investigated from the obtained AMVs. Conclusions are drawn in Section 6.

2. A Review of the Horinouchi et al. (2023) Method

H23 investigated low-level AMVs obtained in the eye of Typhoon Haishen (2020) using research-based special observations with the *Himawari-8*, which were conducted every 30 s. The variable parameters are symbolized as listed in Table 2.

The images were first resampled onto a Cartesian coordinate grid on the azimuthal equidistant projection with respect to the storm center after parallax correction (Bieliński, 2020; Vicente et al., 2002). The AMVs derived in H23 represent storm-relative velocities. This is because the images were sampled with respect to the moving storm center.

High-frequency imaging has the advantage of allowing for easy tracking of small morphological changes in cloud features. However, decreasing the time interval between images (Δt) for a given horizontal resolution (Δh) results in an increase in the nominal discretization error of velocity ($\Delta h/\Delta t$). To overcome this issue and take advantage of high-frequency imaging while minimizing discretization errors, a novel method was introduced in which tracking is performed over multiple steps. H23 used four steps by using five consecutive images taken over 2 min. Additionally, subgrid estimation was employed to further reduce discretization errors. To prevent artifacts from cirrostratus clouds, a screening process was conducted during post-processing.

Table 2
A List of Symbols for the H23 Method Along With Brief Definitions and Values Used in H23

Symbol	Definition	H23 setting
Δt	Time interval between consecutive images.	30 s
Δh	Horizontal resolution of images.	500 m
T_g	Temporal grid spacing of AMVs derivation.	1 min
H_g	Horizontal grid spacing of AMVs derivation.	2 km
R_g	Radial grid spacing of AMVs derivation.	2 km
θ_g	Azimuthal grid spacing of AMVs derivation.	$2\pi/60$ rad
W,H	Template subimage width (W) and height (H), respectively.	11×11 pixels
N_t	Tracking time steps for both forward and backward.	2 steps
C_{th}	Threshold to limit the minimum contrast of template subimage.	0.05 (reflectivity)
V_s	Search range for cloud tracking in velocity dimension.	80 m/s
h_s	Search range for cloud tracking in pixel count.	5 pixels
S_{th}	Threshold to limit the lowest value of the peak cross-correlation coefficient.	0.8
V_c	Threshold to limit the maximum velocity change between consecutive images.	20 m/s
V_d	Threshold to limit the maximum velocity difference between velocities obtained from forward and backward tracking as vectors.	20 m/s
T_{sp}	Threshold to limit the maximum brightness temperature difference between 10.4 and 11.2 μm.	2 K
θ_d	Threshold to limit the maximum angle difference between velocities obtained from forward and backward tracking as vectors.	–
v_{th}	Threshold wind speed for screening by θ_d.	–

Note. The parameters θ_d and v_{th} are not included in the original H23 method, but they are added in this study. The descriptions about them are provided in Section 3.3.

2.1. Cloud Tracking

H23 employed a cloud tracking that relies on the cross-correlation method, similar to the conventional particle image velocimetry. However, it differs in that it utilizes five consecutive images taken over a period of 2 min.

- AMVs were derived at time intervals of T_g on two different types of initial template position grids:
    1) Cartesian grid has a spatial resolution of H_g (km) along both x (eastward) and y (northward) axes.
    2) Polar-coordinate grid samples the radius and azimuth counterclockwise from the east at resolutions of R_g (km) and θ_g (rad), respectively.

    H23 set $T_g = 1$ min, $H_g = 2$ km, $R_g = 2$ km, and $\theta_g = 2\pi/60$ rad, respectively. These grids are used to specify the initial positions of the centers of template subimages, which are used to define AMVs. The tracking of template subimages is always conducted on Cartesian-coordinate images. AMVs derived on the polar-coordinate grid were used when analyzing data on the polar coordinate, such as to show azimuthal means or wavenumber decomposition.

- At every reference time, a template subimage with a size of $W \times H$ pixels in x and y directions is subsampled at each grid point (either in Cartesian or polar-coordinate grids), and it was tracked in a Lagrangian manner for N_t steps forward and backward under the following conditions. The tracking process is carried out only when the subimage has a contrast greater than the threshold C_{th}. H23 set $W = H = 11$, which corresponds to a size of 5 km × 5 km, $N_t = 2$, which corresponds to a duration of 1 min, and $C_{th} = 0.05$ in reflectivity.
    1) The search area for finding the displacement of template subimages across temporally adjacent images is set to cover a velocity range of $-V_s$ to V_s (m/s) in both the x and y directions. Corresponding maximum displacement in pixels (h_s) is calculated as $h_s = \mathrm{ceil}(V_s \cdot \Delta t / \Delta h)$ for both x and y directions, where ceil() is a function that rounds a number up to the nearest integer. To ensure that the correlation maximum is a local peak, an additional one-pixel displacement is tested, resulting in a computation range $\pm(h_s + 1)$ pixels. If the correlation maximum is found on the edge of the search area, that is, at the additional one pixel, the result is rejected.

Table 3
Analysis Information on the TCs Analyzed in This Study

Name (year)	Analysis period	Eye radius	2.5 min	30 s	DS
Haishen (2020)	9 hr from 23:00 UTC 3 Sep. 2020	~35 km	○	○	×
Nanmadol (2022)	8 hr from 23:00 UTC 16 Sep. 2022	~20 km	○	○	○
Lan (2017)	9 hr from 22:30 UTC 20 Oct. 2017	~40 km	○	×	○

Note. The three columns on the right indicate the availability of data, with a circle (cross) symbol indicating availability (unavailability), for 2.5-min interval images, 30-s interval images, and dropsonde (DS) data, respectively.

2) The cloud tracking process is terminated and the result is rejected if the maximum cross-correlation coefficient is below the threshold S_{th}. H23 used a value of $S_{th} = 0.8$ for their analysis.

3) The five-point parabolic fitting around the peak cross-correlation pixel is performed to determine the subpixel destination of the template subimage. The subsequent-step tracking is then carried out using a resampled template subimage centered at this subgrid destination, which is obtained using bilinear interpolation.

4) The tracking result is discarded if either of the two horizontal velocity components changes by more than V_c (m/s) between consecutive tracking steps. Additionally, if the mean velocities obtained from forward and backward tracking differ by more than V_d (m/s) as vectors, the result is also rejected. H23 set $V_c = 20$ m/s and $V_d = 20$ m/s for their analysis.

- AMV is defined as the average of all $2N_t$ velocity vectors. For the H23 setting, a total of four vectors are used, with $N_t = 2$ for each forward and backward tracking.

2.2. Postprocessing

Height assignments of AMVs were performed using the equivalent blackbody temperature method by an infrared window brightness temperature (Fritz & Winston, 1962). The altitude at which the equivalent blackbody temperatures of the infrared window channel matched the temperature profile from the reanalysis data was assigned as the height of the AMV.

In TCs with eyes, the upper troposphere sometimes contains stratiform (cirrostratus) clouds, which can obscure the eyes. The movements of some opaque clouds reflect the flow in the upper troposphere. AMVs derived where nearly transparent clouds mostly reflect the movements of clouds in the boundary layer of the eye. However, these AMVs may have significant parallax errors (Henken et al., 2011; Roebeling & Holleman, 2009) due to the presence of optically thin cirrus clouds, which can lower the brightness temperature. Therefore, it is preferable to exclude these AMVs. To address this issue, H23 used a "split window" technique (e.g., Inoue, 1987) that masks AMVs where the differences in brightness temperature between 10.4 and 11.2 μm are greater than T_{sp}, which was set to 2 K. This technique effectively filters out optically thin upper clouds, and the results were not significantly affected when the threshold was lowered to 1.5 or 1 K. They also applied a masking process based solely on the brightness temperature at 10.4 μm, as needed.

3. Data and Method

In this study, the developed method is applied to Typhoons Haishen (2020), Nanmadol (2022), and Lan (2017). The analysis period, eye radius, and other data availability for these cases are summarized in Table 3. Nanmadol is another typhoon for which, like Haishen, the 30-s imaging was conducted, so AMVs from 2.5-min and 30-s interval image sequences are compared for the two typhoons. Lan was observed only with the operational 2.5-min imaging. Nanmadol and Lan were directly observed using dropsondes released from aircraft by the Tropical cyclones-Pacific Asian Research Campaign for Improvement of Intensity estimations/forecasts (T-PARCII; Ito et al., 2018; Yamada et al., 2021; Hirano et al., 2022) project. The results obtained from 2.5-min observations are examined in relation to the findings from H23 for Haishen. The challenges of deriving AMVs for cases with small eyes, such as Nanmadol (Table 3), are emphasized. Lan is observed to be experiencing a rapid acceleration in the eye, contrasting with the behaviors of Haishen and Nanmadol.

3.1. Data

The data mainly used in this study are visible and infrared images from the *Himawari-8* (Bessho et al., 2016) obtained by a 2.5-min rapid scan observation and research-based special observation conducted every ∼30 s (mostly between 25 and 35 s). Cloud tracking was performed using the visible reflectivity at 0.64 μm, with a resolution of 0.5 km at nadir. The radiance was adjusted to simulate albedo (nondimensional; values up to ∼1.2). For parallax correction (Bieliński, 2020; Vicente et al., 2002) and thin-cloud masking (e.g., Inoue, 1987), the infrared brightness temperatures at 10.4 and 11.2 μm were used, which have resolutions of 2 km at nadir. To correct parallax, the ERA5 (Hersbach et al., 2020), a global reanalysis dataset produced by the European Centre for Medium Range Weather Forecasts, was used to obtain temperature, geopotential, and relative vorticity around TCs. The use of ERA5 in these computations was justified by Slocum et al. (2022). It was assumed that biases in height representations do not affect parallax corrections. The tracks and intensities of TCs analyzed by Japan Meteorological Agency (JMA) and Joint Typhoon Warning Center (JTWC) were obtained from the International Best Track Archive for Climate Stewardship (IBTrACS) best-track dataset (Knapp et al., 2010, 2018). For verification, the 30-s image data for Typhoons Haishen (2020) and Nanmadol (2022) are used. The dropsonde profiles obtained in the eye of Typhoon Lan (2017) on 21 October 2017 and Typhoon Nanmadol (2022) on 17 September 2022 are also used.

3.2. Storm Center Determination and Image Resampling

The parallax shifts (Henken et al., 2011; Roebeling & Holleman, 2009) are corrected from the entire *Himawari-8* data with cloud-top height estimates obtained by equating the infrared brightness temperature to the temperature in the reference vertical profiles obtained from the ERA5 dataset. The best-track storm center lacks the necessary precision for the intended purposes, so the storm centers were manually determined every 30 min by subjectively analyzing the corrected visible and infrared images. The storm center is determined with the intention of corresponding to the center of circulation at the inner edge of the eyewall clouds at altitudes of 4–5 km. The results were then interpolated with time (t) using cubic spline interpolation. The image data were projected onto the azimuthal equidistant projection for the storm center, with a resolution of 0.5 km along the eastward (x) and northward (y) coordinates.

3.3. Method: A TC-Specific Cloud Tracking

A TC-specific cloud tracking method has been developed, and its conceptual diagram is shown in Figure 1. The method considers rotation of template subimages, and it selects candidates by considering the similarity among the AMVs of nearby grid points. The method involves the following eight steps using the projected images:

Step 1: [Image sequence creation] Create image sequences that are rotated in the direction opposite to the rotation in the eye to offset the rotation with respect to time. This is done using constant angular velocities of $\Omega = \Omega_i (i = 1, 2..., N)$.

Step 2: [Cloud tracking] For each sequence, conduct the tracking as in H23 (Section 2) with a narrow search range (i.e., small V_s and h_s). The quality-controlled AMVs are converted to velocities in the non-rotating coordinate system (i.e., $\Omega = 0$) by adding the corresponding tangential velocity ($r\Omega_i\Delta t$) to the tangential component of each AMV, where r is radius from storm center. These AMVs are treated as candidate AMVs, $v_{cand}(x,y,t,\Omega)$, which consist of two horizontal velocity components at each grid point. The peak cross-correlation coefficient in the tracking process is assigned as a "score" for each candidate AMV.

Step 3: [Cloud-top height masking] Keep only the candidate AMVs with cloud-top heights between Z_{min} and Z_{max}, and mask out the rest.

Step 4: [Selection] Select the highest-scoring AMVs from $v_{cand}(x,y,t,\Omega)$ along the Ω axis as the tentative estimates, $v_{tmp}(x,y,t)$.

Step 5: [Median wind computation] Compute the spatiotemporal median wind field, denoted as $v_{med}(x,y,t)$, using a median filter for each horizontal velocity component of $v_{tmp}(x,y,t)$. The filter window has a three-dimensional shape in (x,y,t) dimensions with preset window sizes as described below.

Step 6: [Difference computation] Compute $d_2(x,y,t,\Omega) \equiv \|v_{cand} - v_{med}\|_2$, which is the L2 norm of the difference vector between v_{cand} and v_{med} for each grid point.
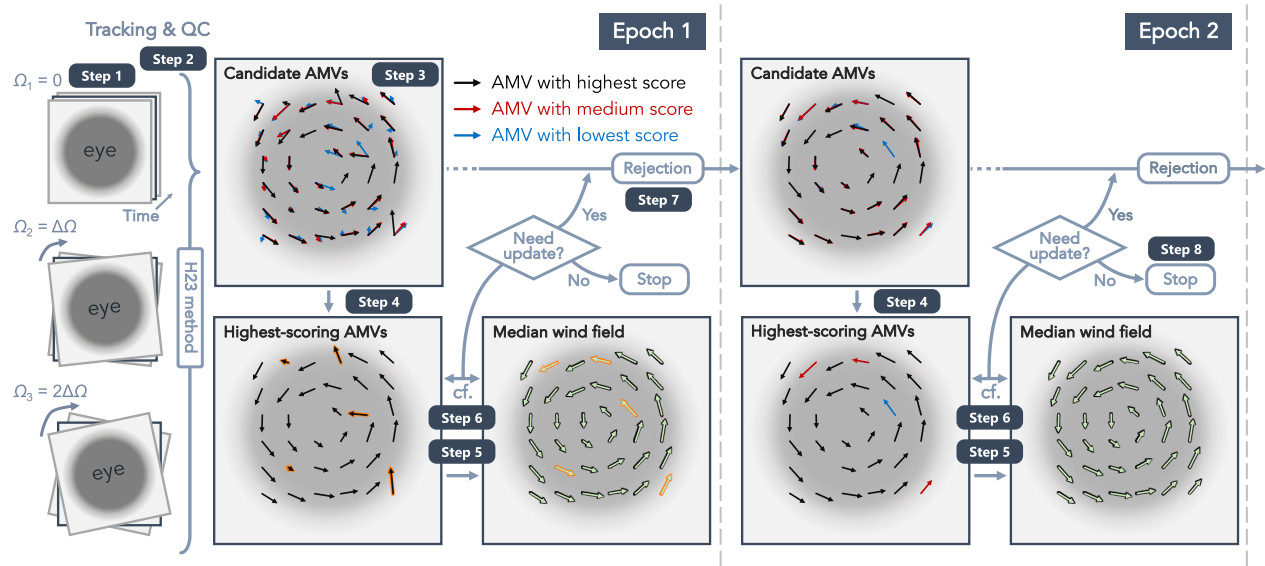
Figure 1. A schematic diagram illustrating the procedure of the TC-specific cloud tracking method. The gray shading represents a visible image around the eye of a TC, with the eye depicted as a dark area and the top of the eyewall cloud displayed as a white area. The thin vectors are AMVs, referred to as candidate AMVs, obtained from three image sequences (one original, two counter-rotated at different angular velocities). The vectors are colored black, red, and blue based on their score, which is determined by the cross-correlation coefficient. The thick light-green vector represents the median wind. It is calculated by applying a spatiotemporal median filter to the AMVs with the highest scores. The orange-bordered vectors indicate pairs that exhibit a large difference between the highest-scoring AMVs and the median wind at the same grid point. If such vectors are present, it indicates the need to proceed with a rejection process. The rejection process involves discarding all candidate AMVs that have a large difference from the median wind at the same grid point. After the rejection process, if the difference between the highest-scoring AMVs and the median wind is not large at all grid points, the highest-scoring AMVs are considered the final AMVs. If the difference is large, the process continues to the next rejection process.

Step 7: [Rejection] If there is a candidate AMV in v_{cand} that satisfies the criteria $d_2 \geq d_{th}$ or $d_2 \geq d_c \times \|v_{med}\|_2$, where $\|v_{med}\|_2$ is the L2 norm (wind speed) of v_{med} for each grid point, reject that candidate from v_{cand} and return to Step 4 using the updated v_{cand}. If not, proceed to Step 8.

Step 8: [Finalization] Stop the process and use the resulting v_{tmp} as the final estimates (v_{final}).

The symbolized variables are listed in Tables 2 and 4. The developed method is unique in that it selects and combines AMVs with high correlation coefficients from the candidate AMVs obtained from multiple counter-rotating image sequences.

The counter rotation conducted for the entire images in Step 1 acts to rotate template subimages. Since the final results are selected locally from the different rotations, the method acts to consider local rotation depending on both time and position. In this step, Ω_i are set as $\Omega_i = \Omega_{min} + (i-1)(\Omega_{max} - \Omega_{min})/(N-1) = \Omega_{min} + (i-1)\Delta\Omega (i = 1, 2, \ldots, N)$. While the Ω_{max} should be set sufficiently large, it is advisable to keep it within realistic limits to avoid erroneously generated AMVs. The interval $\Delta\Omega$ should be set sufficiently small, and empirically, a value of approximately 1.0×10^{-3} rad/s is sufficient for small eye with a radius of ~20 km or less, while a value of 0.5×10^{-3} rad/s is sufficient for larger eye. Since the striations rapidly deform with time (Section 1), the threshold of cross-correlation coefficient (i.e., S_{th}) should be set relatively low (e.g., 0.7).

In Step 2, the cloud tracking method developed in H23 is employed for each image sequence. In this study, H23 method is slightly modified as follows:

- An optional quality control is added to the H23 method, where AMVs are rejected if the directions of the velocities obtained from forward and backward tracking differ by more than θ_d, given that either the forward or backward wind speed is greater than or equal to v_{th}.
- For comparison purposes, the final AMVs are obtained by making the two velocity vectors connecting the start and end points of each forward and backward tracking, and then averaging the two vectors. Note that the H23 obtained the final AMVs by averaging the vectors of N_t steps of forward and backward tracking separately and then averaging the two means.

Table 4
A List of Symbols for the Developed Method

Symbol	Definition
r	Distance from storm center
Ω_i	Preset angular velocities to create counter-rotating image sequences ($i = 1, 2, \ldots, N$).
Ω_{min}	The minimum value of Ω_i.
Ω_{max}	The maximum value of Ω_i.
$\Delta\Omega$	The equally spaced intervals of Ω_i.
v_{cand}	Candidate AMVs passed the quality control of H23 method for each image sequence.
Z_{min}	Threshold to limit the minimum cloud top height for masking of v_{cand}.
Z_{max}	Threshold to limit the maximum cloud top height for masking of v_{cand}.
v_{tmp}	Tentative AMV estimates obtained from v_{cand}.
v_{med}	Median filtered AMVs obtained from v_{tmp}.
d_2	L2 norm of the difference vector between v_{med} and v_{cand} for each grid point.
d_{th}	Threshold to limit the maximum d_2 for rejection of v_{cand}.
d_c	Coefficient to be multiplied by the L2 norm of v_{med} for rejection of v_{cand}.
v_{final}	Final AMVs after the quality control.
T_w	Temporal window size for median filter.
H_w	Horizontal window size for median filter.
τ_{stri}	Temporal window size to compute the velocity contrast of v_{final} for detection of striations.
v_{stri}	Threshold to limit the maximum velocity contrast for detection of striations.
Z_{stri}	Threshold to limit the maximum cloud top height for detection of striations.
Ω_{stri}	Threshold to limit the minimum Ω_i for the striation grids.

- In H23, AMVs were derived using two types of initial template position grids (Cartesian and polar co-ordinates), while we only utilize the Cartesian grid for the reason described in the following paragraph. For azimuthal averaging and azimuthal wavenumber decomposition, we first spatially smooth the wind field using a 4 km × 4 km Gaussian kernel with a standard deviation of 0.67 km. Then, we resample the obtained AMVs on the Cartesian grid to the polar coordinates using bilinear interpolation.

From Step 5, candidate estimates that are not smooth with the surrounding flow are rejected based on comparison with the median wind. Grid point distribution for the median filter (Step 5) should be nearly uniform, so we use the Cartesian grid. The shape and size of the window is determined by setting H_w in x and y axes and T_w in time axis. If the window size is too large, the median wind may not be effective as a local reference wind. Since appropriate parameter values may vary depending on the TC case, it is prudent to try several values.

The iterative updating approach using median-filtered wind fields is similar to a method developed to resolve directional ambiguities in scatterometer-derived wind fields (Schultz, 1990). This method selects the closest wind direction from multiple candidate directions by comparing them to the median direction. The computation of the median direction and selection process continues until the selected wind vectors remain unchanged between iterations or until a maximum number of iterations is reached. Unlike our method, this approach does not incorporate a rejection process, resulting in missing data (no-solution) not being newly assigned through the process. In our problem, as there is no assurance that the candidate AMVs in a certain grid point have accurate estimates, introducing a "no-match" (no-solution) based on rejection is effective.

Our approach is also similar to the relaxation labeling, also known as the relaxation method, which is used for assigning labels to objects or scenes (Rosenfeld et al., 1976). The relaxation method has been utilized to correct erroneous template matching for optical flow detection and particle tracking velocimetry (e.g., Horinouchi et al., 2017). In the relaxation method, the "labels" are assumed to be independent, meaning that the candidate AMVs at a grid point should have distinct or well-separated destinations. However, the candidate AMVs in this study are not necessarily independent as they often include nearly the same destinations. In such cases, the

relaxation labeling method can erroneously weigh the multiply selected candidates (Horinouchi et al., 2017). Our approach of iteratively rejecting improbable candidates effectively addresses our problem.

While the above procedure allows for obtaining low-level AMVs in the eye, incorrect AMVs can often be obtained on "striations" or "finger-like features" (Bluestein & Marks, 1987; Aberson et al., 2006; Marks et al., 2008; TH20; Yamada et al., 2021). Intense TCs often have the striations in their eyes. The striations were examined in TH20 as having the following characteristics:

- They exist at inner edge of the eyewall clouds from the lower to middle levels.
- Their cloud top heights have a wavy pattern that regularly rises and falls in the azimuthal direction.
- They become inclined due to the vertical shear of the tangential wind.
- The radial shear of tangential wind is greater inside the striations due to its higher angular velocity compared to the region inside it.

Around the inner edge of the eyewall cloud, where the cloud top height varies greatly along the radial direction, there is little continuity with the motion around the striations. The wavy pattern can easily lead to incorrect tracking, and the cloud deformation caused by vertical shear leads to loss of cloud similarity between consecutive images. Therefore, tracking the clouds of the striations is a very challenging task. Specifically, the incorrect AMVs derivation occurs when cloud-tracking points that were on a certain striation switch to a different following striation, a common artifact known as optical flow temporal aliasing (Fleet & Weiss, 2006). Each individual striation is generated sequentially at a certain position and deformed by the local vertical shear of the tangential wind with time elapsed from its generation (see Figure 5e in TH20). Therefore, a template subimage on a striation at a certain time has a decrease in the cross-correlation coefficient due to the deformation with time. In contrast, a subsequent younger striation has not yet been deformed, resulting in a switching of the striation.

Striations have been taken into consideration, and an optional additional process is presented that establishes a lower limit on Ω_{min} for grids where striations are present. The grids on the striations are identified based on the cloud tracking results described above. These processes are summarized in the following two steps:

Step A1: The grids that satisfy both of the following conditions in the obtained wind field are considered *striation grids*:

- The velocity contrast, which is the difference between the maximum and minimum velocities within a time width τ_{stri} for $\|v_{final}\|_2$, where $\|v_{final}\|_2$ is the L2 norm (wind speed) of v_{final} for each grid point, is greater than or equal to v_{stri}.
- The cloud top height is lower than Z_{stri}.

Step A2: At the striation grids, reject the results obtained at $\Omega_i < \Omega_{stri}$ and restart the above procedure from Step 4.

The setting for v_{stri} and Ω_{stri} should be tested with several values as they depend on the velocity of striations, the radius of striations, the azimuthal spacing of each striation, and the search range for cloud tracking. An example of configuration values for these parameters is shown in the following section.

3.4. Evaluations for Derived AMVs

In Sections 4.1 and 4.2, AMVs obtained from 2.5-min and 30-s interval images are compared. The comparison is performed for each grid point and for the azimuthally averaged field. These comparisons are carried out after restricting the grid points to only those where quality-controlled AMVs are obtained in common for both 2.5-min and 30-s observations. To ensure consistency throughout these comparisons, the AMVs are then resampled on polar coordinates using bilinear interpolation after spatial smoothing with a 4 km × 4 km Gaussian kernel with a standard deviation of 0.67 km. Any missing data in the resampled AMVs are linearly interpolated along the azimuth axis. Note that the comparison at each grid point is also performed using the resampled data.

In Sections 4.2 and 4.3, AMVs are evaluated by comparing them with the in-situ GPS dropsonde observations. These observations provide the most reliable measurements, which allow us to evaluate the accuracy of the obtained AMVs. According to H23, the AMVs near the center of the eye, where clouds are typically dispersed, are expected to reflect the average horizontal velocities across the boundary layer excluding the near-surface layer. Except near the center (or where cloud top heights are around 3 km or higher), clouds are densely packed, so the

AMVs are expected to reflect motion of brightness features appearing near the top of the clouds. Since the dropsondes released in the eye fell into the dispersed cloud region, we compare the AMVs with mean horizontal velocities across the boundary layer except the near-surface layer. From the observed dropsonde profile, the boundary layer can be identified as a low-level moist layer beneath a dry free atmosphere (e.g., Yamada et al., 2021). We define the top of the boundary layer as the altitude where the relative humidity, recorded by a falling dropsonde, first exceeds 80% (or 60% if the former is not reached). For comparison with AMVs, the reference position, time, and wind speed of a falling dropsonde were determined by averaging the first 80% of the observing period from the boundary layer top to the surface. In the boundary layer, the vertical wind shear is shown to be relatively weak, so the choice of the computation range has minimal effect on the computation of the reference wind speed. Prior to the comparison, the AMVs are first smoothed spatially using a 4 km × 4 km Gaussian kernel with a standard deviation of 0.67 km. Then, the AMV used for the comparison is obtained by linear interpolation at the reference position and time of the dropsonde.

4. Results and Evaluations for AMVs Derivation

The proposed method is applied to three Typhoons Haishen (2020), Nanmadol (2022), and Lan (2017) with the parameters listed in Table 5. Since cloud tracking is relatively straightforward with 30-s interval images, the parameters are set to be stricter than those for cloud tracking with 2.5-min interval images.

4.1. AMVs for Typhoon Haishen (2020)

In this section, the obtained AMVs in Typhoon Haishen (2020) and evaluation of them are provided. The best-track position and intensity of Haishen, along with the environmental vertical wind shear and the TC translation, are shown in Figure 2. The AMVs derived from the 2.5-min interval images (Figure 3a) are less dense than those obtained from the 30-s interval images (Figure 3b). Nonetheless, they still offer a wide range of valid AMVs.

Within a radius of 25 km, the tangential and angular velocities obtained from both intervals are relatively similar (Figure 4). In contrast, beyond a 25-km radius, there are areas where the differences in tangential velocities derived from 2.5-min and 30-s observations are relatively large. This is due to the lower sampling density in those regions (Figure 3) and the challenges in accurately estimating wind speed around striations in the 2.5-min observations. Especially near rapidly deforming striations, there seem to be numerous missing AMVs, particularly in the northeast quadrant of Figure 3a, despite the application of special treatment to address this issue (Section 3.3). Note that in the vicinity of eyewall clouds where there are large variations in cloud-top height along the radius, the azimuthal-mean winds should not be interpreted as representing a nearly constant altitude due to the large variability in cloud-top heights of the AMVs used for the average.

The angular velocity obtained from both 2.5-min and 30-s intervals are characterized by the oscillating signals in time, which is consistent with the algebraically growing wavenumber-1 disturbance shown by H23. If this wavenumber-1 feature is centered to the storm center, the signal does not appear in the azimuthally averaged field. However, according to H23, the time-mean low-level circulation center of Haishen was shifted rearward (southeastward) of translation (northwestward), so the signal was not canceled out. This signal is evident in terms of angular velocity, but it is also present in the radial velocity, as well as the tangential velocity. The overall speed up of the low-level rotation in the eye, which can be explained by the angular momentum transport by the wavenumber-1 disturbance, was reported by H23. The wavenumber-1 features in the eye of Haishen is examined more in Section 5.1.

The AMV acquisition rate, defined as 1 if quality-controlled AMVs were obtained at all grid points passing through the cloud-top-height masking (Step 3 in Section 3.3) and split-window masking (Section 2.2), was 0.72 for 30-s observations and 0.38 for 2.5-min observations.

In the evaluation for each grid point (Figure 5a), more than 60% of the AMVs had absolute wind speed differences within 2 m/s, while more than 80% of the AMVs had the differences within 4 m/s, and more than 90% of the AMVs had the differences within 7 m/s. About 5% of the AMVs had differences of 9 m/s or higher, mainly as a result of estimation errors related to the striations in the 2.5-min interval images. Despite the presence of some erroneous AMVs in the 2.5-min interval images, overall differences are reduced through spatial and temporal averaging. Comparing the azimuthal-mean and 10-min running mean winds (Figure 5b), more than 70% of the winds had differences within 2 m/s, and 90% had differences within 4 m/s. The evaluation metrics, including

Table 5
A List of Setting Parameters for Typhoons Haishen (2020), Nanmadol (2022), and Lan (2017) With 30-Sec or 2.5-min Interval Observations

Symbol	30-s observations		2.5-min observations		
	Haishen	Nanmadol	Haishen	Nanmadol	Lan
Δt	30 s		2.5 min		
Δh	500 m		500 m		
T_g	30 s		2.5 min		
H_g	1 km		1 km		
W,H	7×7 pixel		7×7 pixel		
N_t	5 steps		1 step		
C_{th}	0.03		0.03		
V_s	10 m/s		10 m/s		
h_s	5 pixels		3 pixels		
S_{th}	0.8		0.7		
V_c	20 m/s		N/A		
V_d	20 m/s		20 m/s		
T_{sp}	2 K		2 K		
θ_d	N/A	N/A	60°		
v_{th}	N/A	N/A	5 m/s		
Ω_{min}	0.0×10^{-3} rad/s		0.0×10^{-3} rad/s		
Ω_{max}	3.0×10^{-3} rad/s	5.0×10^{-3} rad/s	3.0×10^{-3} rad/s	5.0×10^{-3} rad/s	2.5×10^{-3} rad/s
$\Delta\Omega$	0.5×10^{-3} rad/s	1.0×10^{-3} rad/s	0.5×10^{-3} rad/s	1.0×10^{-3} rad/s	
Z_{min}	0 km		0 km		
Z_{max}	6 km		6 km		
d_{th}	10 m/s		10 m/s		
d_c	0.5		0.5		
T_w	10 min		20 min		
H_w	6 km		6 km		
τ_{stri}	N/A	N/A	1 hr		
v_{stri}	N/A	N/A	15 m/s	10 m/s	20 m/s
Z_{stri}	N/A	N/A	6 km		
Ω_{stri}	N/A	N/A	1.5×10^{-3} rad/s	3.0×10^{-3} rad/s	

Note. Text "N/A" indicates an unused parameter. Only values that differ from column 2 are shown in column 3, and only values that differ from column 4 are shown in columns 5–6.

results for azimuthal averaging, 10-min averaging, and both applied together are summarized in Table 6. The root-mean-square difference (RMSD) in tangential velocity decreased from 5.2 m/s to 2.7 m/s, and in radial velocity from 2.9 m/s to 1.2 m/s, through both averaging processes. Table 6 indicates that the reduction in difference of tangential velocity was primarily due to the azimuthal averaging. Through azimuthal averaging, the correlation coefficient increased in tangential velocity but decreased in radial velocity. This decrease was due to the difficulty of quantifying azimuthal-mean radial velocity, as it represents a small residual from the predominant variation at wavenumber 1.

4.2. AMVs for Typhoon Nanmadol (2022)

In this section, the obtained AMVs in Typhoon Nanmadol (2022) and evaluation of them are provided like the previous section. The best-track position and intensity of Nanmadol, along with the environmental vertical wind shear and the TC translation, are shown in Figure 6. According to the JTWC best-track intensity estimation,
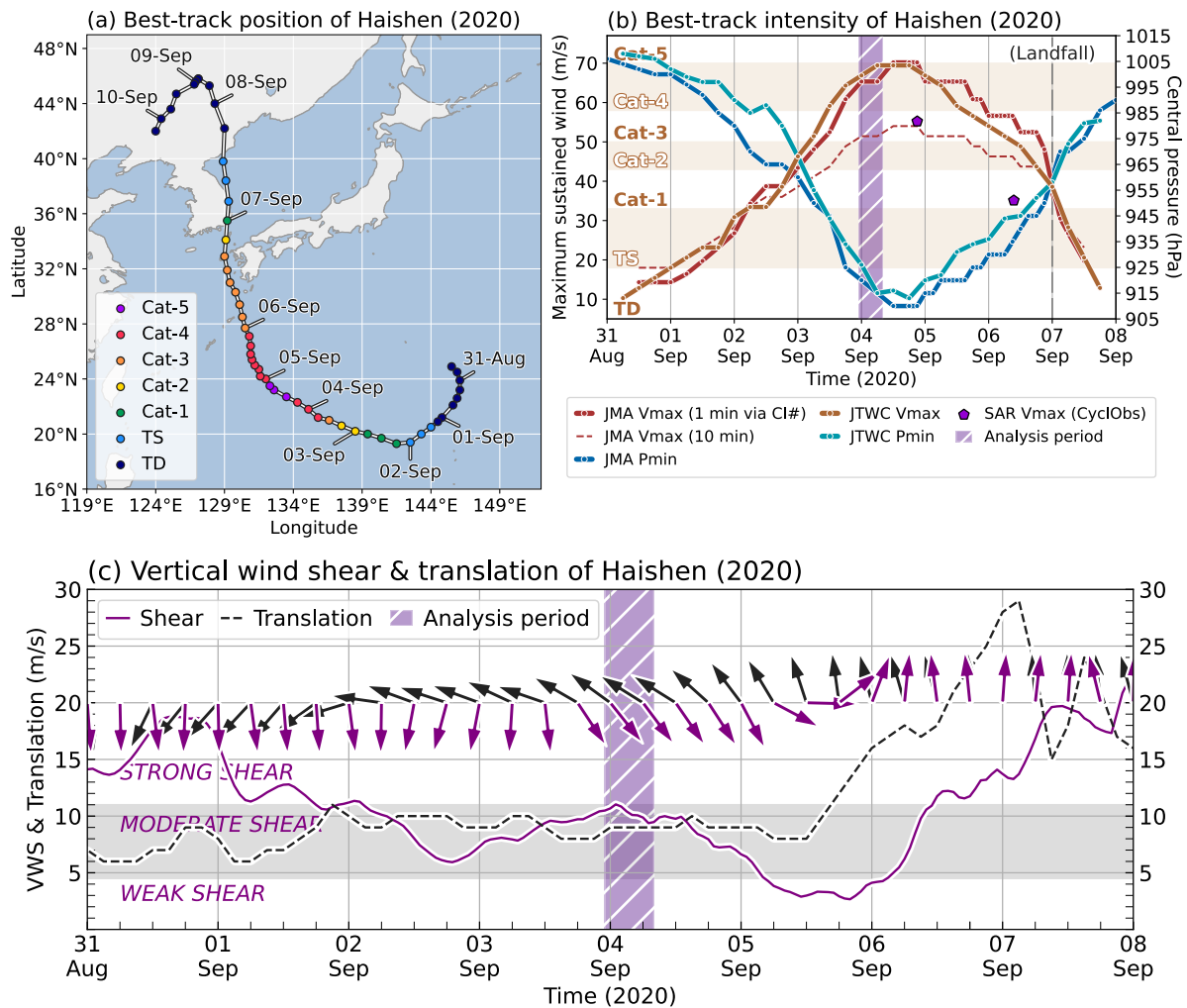
Figure 2. (a) The JMA best-track positions of Typhoon Haishen (2020). The dot color indicates the Saffir-Simpson category (Simpson, 1974) based on the JMA best-track intensity. (b) The JMA (JTWC) best-track intensity, where the blue (cyan) solid curve represents the central pressure (hPa), and the red (brown) solid curve represents the 1-min maximum sustained wind speed (m/s). The original JMA 10-min maximum sustained wind (red broken) were converted to 1-min wind (red solid) using CI-number method proposed by Mei and Xie (2016); the 10-min wind are converted back to Dvorak CI number using the Koba table (Koba et al., 1990), which is then used to calculate 1-min wind using the Dvorak table (Dvorak, 1984). Purple pentagon indicates the maximum instantaneous wind speed retrieved using C-band SAR observation. The black long-dashed line indicates the landfall time. (c) Time series of the vector and magnitude of both the environmental vertical wind shear (purple; m/s) between 200 and 850 hPa and the TC translation (black; m/s). The range of moderate shear strength defined by Rios-Berrios and Torn (2017) is shaded. The vertical wind shear is defined as the difference between 200 and 850 hPa mean winds calculated for an annulus area of 200–800 km in radius from the maximum 850-hPa relative vorticity position near the center of the best-track position using the ERA5 isobaric data. The TC translation speed and direction were obtained from the IBTrACS best-track data. The purple shading indicates the analysis period.

Nanmadol had a comparable maximum wind speed and a smaller eye about a half as Haishen (Table 3). Thus, the angular velocity in the eye is about twice as high, making it a challenging case for cloud tracking.

As in the results in Haishen, the AMVs obtained from the 2.5-min interval images (Figure 7a) are less dense than those obtained from the 30-s interval images (Figure 7b). Tangential and angular velocities obtained from the 2.5-min images (Figures 8a and 8b) are higher than those from 30-s images at certain times within a 10-km radius, while lower beyond that radius.

The angular velocity (Figure 8b) within an 8-km radius obtained from 30-s images intensified from ∼03:30 UTC, while that obtained from 2.5-min images intensified from ∼02:00 UTC. Although the timing is different, the gradual intensification of the rotation in the eye, similar to Haishen, was observed in the AMVs obtained from both image sequences. Frequent cloud generation and dissipation near the central region in the eye of Nanmadol
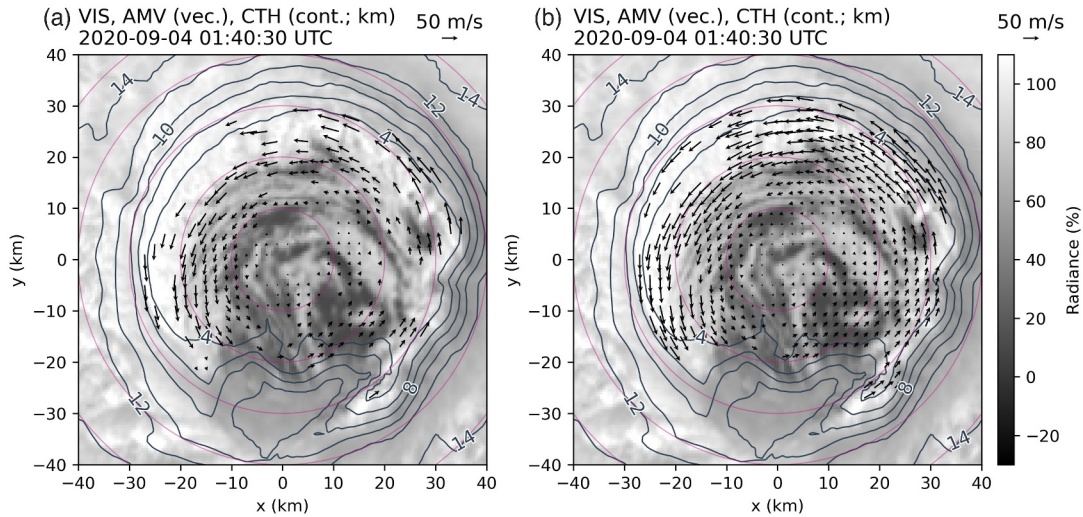
Figure 3. Example of AMVs in Typhoon Haishen (2020) obtained from the (a) 2.5-min and (b) 30-s interval image sequences using the Cartesian grid (vectors) overlaid on the reflectivity (gray shading) at the central time of tracking at 01:40:30 UTC 4 September 2020. The AMVs were derived at $H_g = 1$ km intervals, but they are plotted at 2 km intervals for visualization. The length of the arrow on the upper-right corner corresponds to 50 m/s. The contours represent the cloud-top height (km) obtained from 10.4-μm infrared brightness temperature and the ERA5 reanalysis. The purple circles are drawn at intervals of 10-km radius.
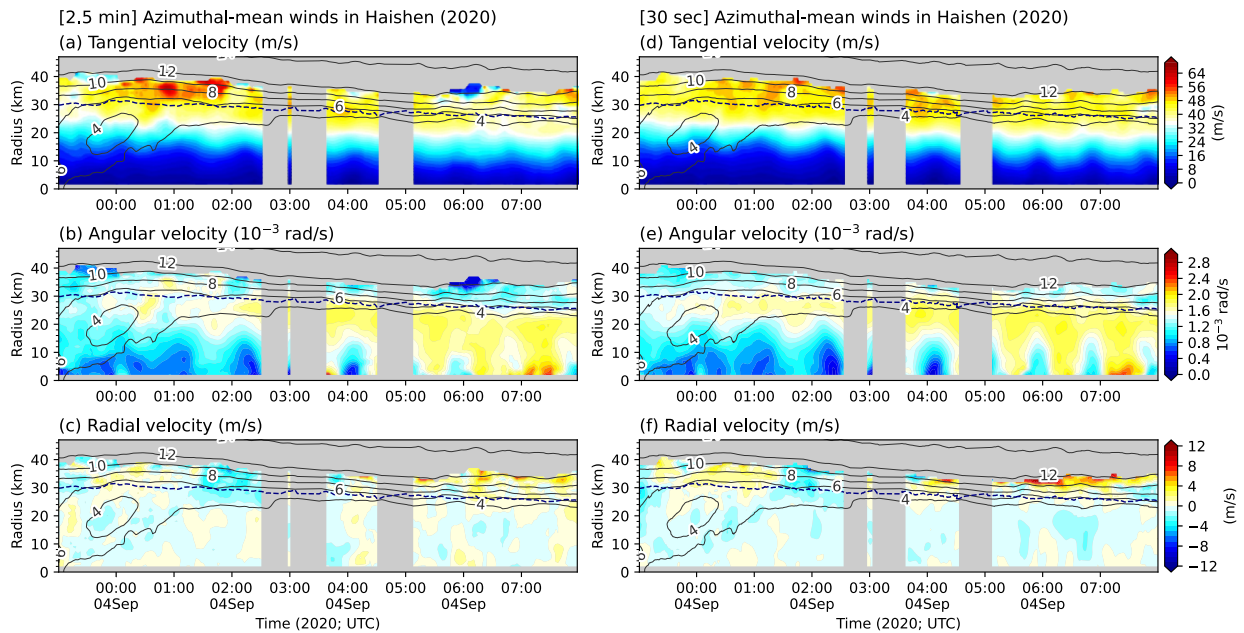
Figure 4. Azimuthal-mean and 10-min running-mean (a),(d) tangential velocity, (b),(e) angular velocity and (c),(f) radial velocity in the eye of Typhoon Haishen (2020) obtained from (left) 2.5-min and (right) 30-s interval image sequences. The black contours represent the azimuthal-mean cloud-top height (km). The blue dashed contour indicates the sea-surface (10-m altitude) RMWs estimated from the GMS-measured eye radius when the storm has a clear eye, using the method proposed by Tsukada and Horinouchi (2023). To produce this figure, we first spatially smoothed the AMVs on the Cartesian grid using a 4 km × 4 km Gaussian kernel with a standard deviation of 0.67 km. Then, we resampled the AMVs to polar coordinates and linearly interpolated any missing data along the azimuthal axis. Finally, we averaged azimuthally.
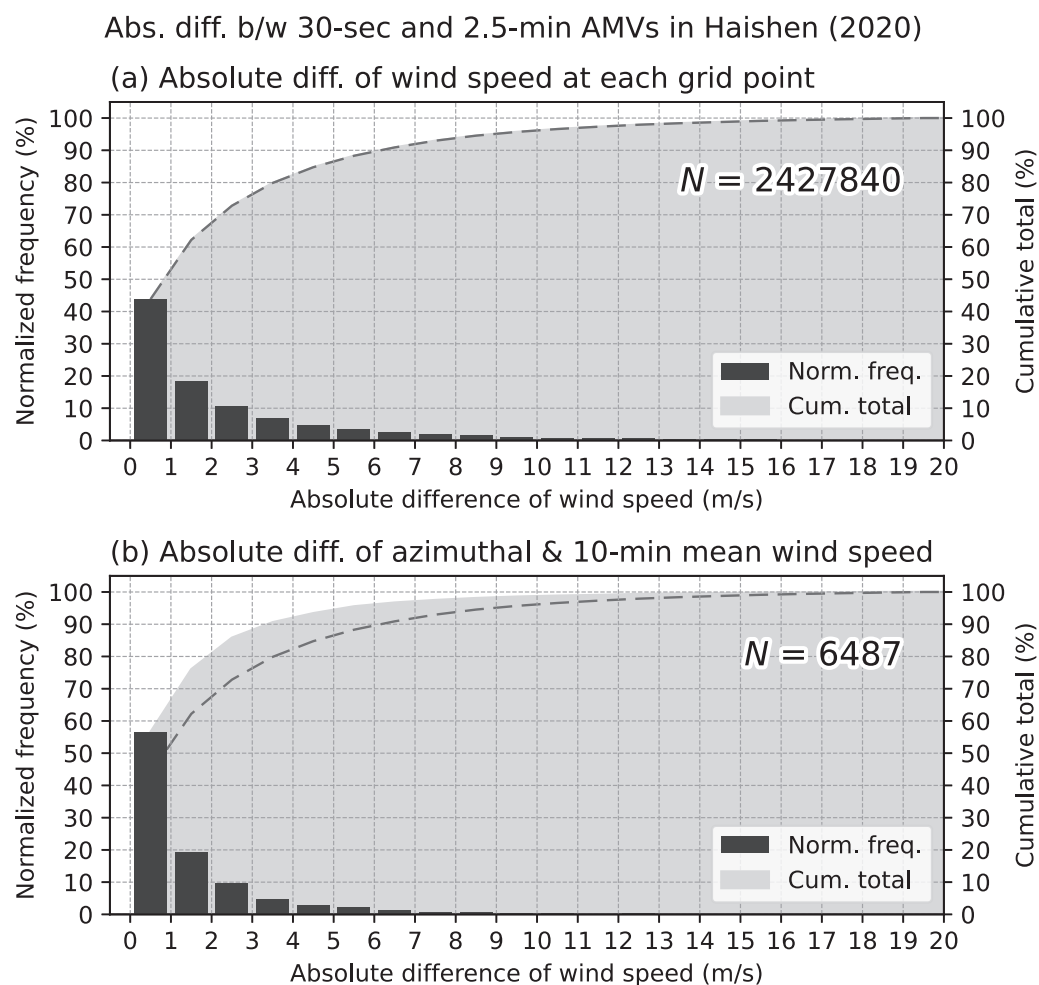
Figure 5. Normalized histogram of absolute wind speed differences for (a) each grid point and (b) azimuthal-mean and 10-min running-mean winds in the eye of Typhoon Haishen (2020). The bar indicates the normalized frequency (%) for a corresponding difference at intervals of 1 m/s. The gray shading indicates the cumulative total percentage, and the black dashed line in panel (b) represents the cumulative total percentage from panel (a). The sample size for each panel is written in the upper-right corner.

was observed starting around 02:00 UTC. This is thought to have resulted in a decreased acquisition rate of quality-controlled AMVs and led to a positive bias in the azimuthally-averaged tangential wind.

As in the previous section, AMVs obtained from 2.5-min observations are compared with those from 30-s observations. The AMV acquisition rate was 0.68 for 30-s observations and 0.33 for 2.5-min observations. When comparing at each grid point (Figure 9a), more than 65% of the AMVs had absolute wind speed differences within 3 m/s. With the azimuthal-mean and 10-min running-mean winds (Figure 9b), more than 75% of the winds had differences within 3 m/s. The overall consistency was lower compared to that in Haishen. In the evaluation metrics shown in Table 7, the tendency of difference reduction is qualitatively consistent with that of Haishen (Table 6), but the RMSDs in tangential velocity are larger for Nanmadol. These results highlight the difficulty in cloud tracking for storms with small eyes and high angular velocities, such as Nanmadol, and suggests the need for shorter imaging intervals.

As described in Section 3, in-situ observations of Nanmadol were conducted using GPS dropsondes released from aircraft as a part of the T-PARCII project. In the vertical profiles of relative humidity and wind speed observed by dropsondes (Figure 10), all of these profiles exhibit a sudden increase in relative humidity at pressure levels below 700 hPa, followed by a relatively constant humidity below that, indicating the top of the boundary layer. In the boundary layer, the vertical wind shear was relatively weak. To compare with the AMVs, the reference position,

Table 6
Evaluations of the Differences Between the AMVs Derived From 2.5-min and 30-Sec Interval Images in Typhoon Haishen (2020)

	Tangential velocity				Radial velocity			
	(a)	(b)	(c)	(d)	(a)	(b)	(c)	(d)
cc	0.96	0.99	0.96	0.99	0.90	0.66	0.93	0.65
Bias (m/s)	0.0	0.0	−0.3	−0.3	0.1	0.1	0.0	0.0
RMSD (m/s)	5.2	2.9	5.1	2.7	2.9	1.3	2.3	1.2
MAD (m/s)	2.9	1.6	2.6	1.5	1.8	0.8	1.4	0.7

Note. Tangential and radial components derived from 2.5-min interval images are evaluated by comparing them to those from 30-s interval images for (a) each grid point, (b) azimuthal-mean velocities, (c) 10-min running-mean velocities, and (d) azimuthal-mean and 10-min running-mean velocities. Row 1 ("cc") indicates the correlation coefficient. Rows between 2 and 4 indicate the bias (m/s), root-mean-square differences (RMSD) (m/s), and mean-absolute differences (MAD) (m/s), respectively. A positive bias indicates an overestimate (i.e., 2.5-min interval AMVs >30-s interval AMVs), and vice versa.

time, and wind speed of a dropsonde were determined by averaging across the boundary layer (gray-shaded layer in Figure 10) excluding the near-surface layer.

The AMVs obtained from 2.5-min interval images had a root-mean-square error (RMSE) of 2.1 m/s for the tangential velocity (Figure 11a) and 2.7 m/s for the radial velocity (Figure 11b), while the AMVs obtained from 30-s interval images had an RMSE of 1.5 m/s for the tangential velocity (Figure 11c) and 1.9 m/s for the radial velocity (Figure 11d). Using images at 30-s intervals makes it easy to track clouds in consecutive images, but errors can arise when it does not reflect the wind. We speculate that the apparent cloud movement due to cloud generation and dissipation is a major contributing factor to the errors in AMVs obtained from 30-s images. The above comparisons demonstrate that relatively accurate AMVs can be obtained even with a 2.5-min interval image sequence.

4.3. AMVs for Typhoon Lan (2017)

This section provides the AMVs obtained from only 2.5-min observations in Typhoon Lan (2017) and evaluates them by comparing them to the dropsonde observations. The best-track position and intensity of Lan, along with the environmental vertical wind shear and the TC translation, are shown in Figure 12. According to the JTWC best-track intensity estimation, Lan had a comparable maximum wind speed as Haishen and Nanmadol, but its radius was about 5 km larger than that of Haishen (Table 3).

An example of obtained AMVs and corresponding angular velocities obtained from 2.5-min interval image sequence at 00:32 UTC 21 October 2021 are shown in Figure 13. At that time, distinct striations near a 30-km radius in the northeast quadrant are shown in the visible image. The angular velocities (Figure 13b) obtained on the striations are about 1.75×10^{-3} rad/s, which is consistent with the subjective analysis conducted in TH20. The angular velocity of the striations is higher than that of the inner region and also higher when compared to other azimuths at the same radius.

In the beginning of the analysis period, the angular velocity within a radius of 20 km was about half the magnitude of the angular velocity inside the inner edge of the eyewall (Figure 14b). After experiencing an increase in angular velocity from 00:00–01:00 UTC, it subsequently returned to its original angular velocity. Around 03:00 UTC, the angular velocity rapidly increased again and maintained the angular velocity of about 1.5 times the previous value thereafter. In Sections 5.2 and 5.3, it is demonstrated that the transport of angular momentum by the mesovortices played an important role in the rapid increase of the rotation.

As in Nanmadol, Lan was also observed using GPS dropsondes as a part of the T-PARCII project. The obtained AMVs are evaluated using the dropsonde observations as in the previous section. As in Nanmadol, the vertical wind shear in the boundary layer was relatively weak (Figure 15). The AMVs had an RMSE of 1.7 m/s for the tangential velocity (Figure 16a) and 1.1 m/s for the radial velocity (Figure 16b). The comparison showed that relatively accurate AMVs were obtained with the 2.5-min observations for Lan.

5. Asymmetric Features in the Eye of Tropical Cyclones

In this section, the asymmetric features in the eye of the three TCs revealed by obtained AMVs are documented. We focus on the algebraically growing wavenumber-1 disturbances and the angular momentum transport associated with mesovortices.

5.1. Algebraically Growing Wavenumber-1 Disturbances

As described in Section 1, H23 found an algebraically growing wavenumber-1 disturbance in Haishen. The disturbance is well reproduced in the AMVs obtained from 2.5-min interval images (Figures 17a–17e). Note that the average angular velocity is stronger in the northwest quadrant (Figures 17c and 17h) and weaker in the southeast quadrant (Figures 17e and 17j) due to not defining the TC center relative to the overall low-level circulation center as done in H23.
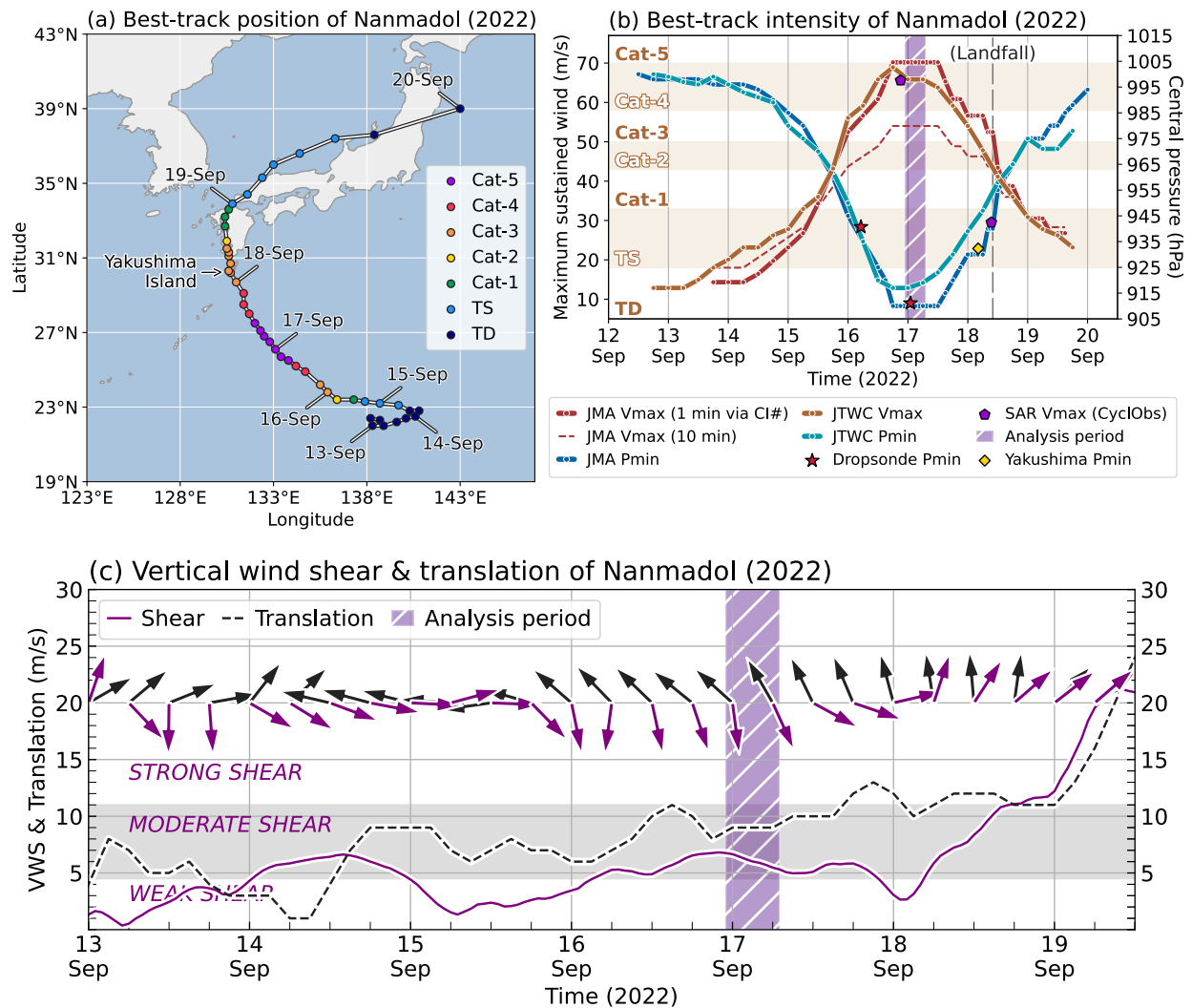
Figure 6. As in Figure 2, but for Typhoon Nanmadol (2022). The red star indicates the central pressure obtained from the T-PARCII dropsonde observation. The yellow diamond indicates the minimum sea-level pressure recorded at the Yakushima weather station (located at 30.231°N, 130.395°E, 37 m above mean sea level) on Yakushima Island at 04:10 UTC 18 September 2022.

The wavenumber-1 disturbance was also found in the eye of Typhoon Nanmadol (Figure 18). In the eye of Nanmadol, the angular velocities in each quadrant oscillated with a period of around 30 min. The corresponding angular velocity is around 3.49×10^{-3} rad/s, which is close to the maximum azimuthally-averaged angular velocity inside the inner edge of the eyewall. This observation is also consistent with theoretical predictions as in Haishen. The slower rotation in the southeast quadrant and faster rotation in the northwest quadrant inside the inner edge of the eyewall can be explained by the northwestward TC translation (Figure 6) as in Haishen.

The wavenumber-1 disturbance was also found in the eye of Typhoon Lan (Figure 19). In the eye of Lan, the angular velocities in each quadrant oscillated with a period around 1.5 hr; the corresponding angular velocity is around 1.16×10^{-3} rad/s, which is close to the maximum azimuthal-mean angular velocity inside the inner edge of the eyewall. Unlike Haishen and Nanmadol, the increase in the azimuthal-mean angular velocity in the eye of Lan (Figure 19a) was achieved relatively quickly, within a short period of 1 hr (02:30–03:30 UTC). The next section explores the role of mesovortices in the rapid speed up in the eye of Lan.
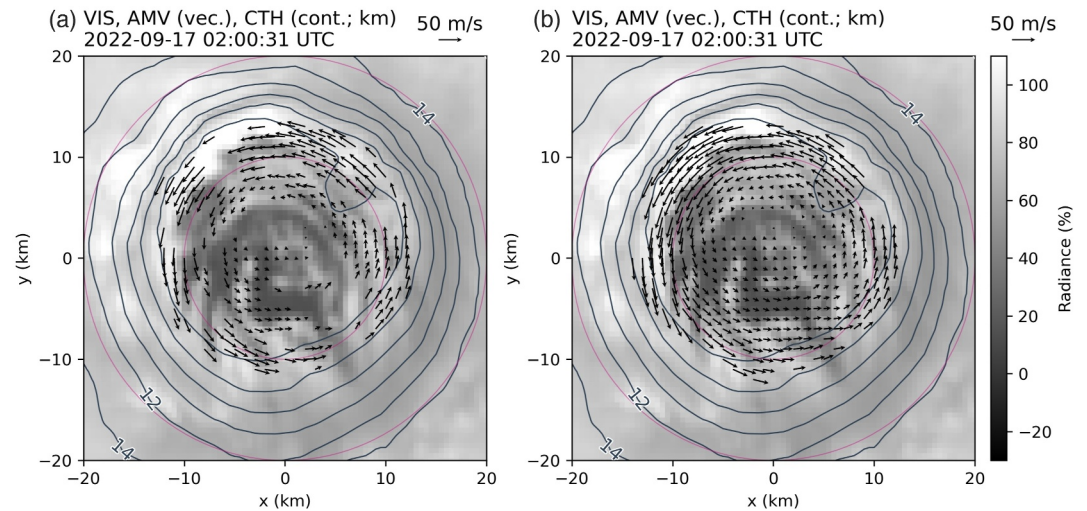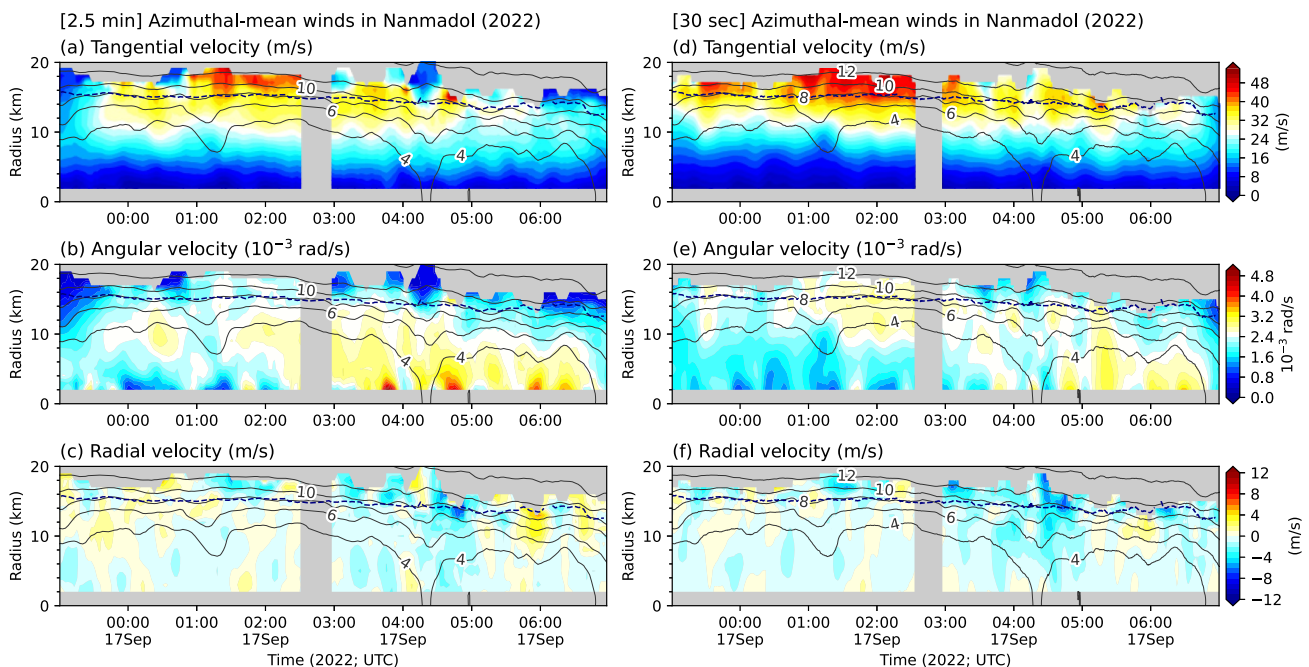
Figure 7. As in Figure 3, but for Typhoon Nanmadol (2022) at 02:00:31 UTC 17 September 2022. The AMVs are plotted at $H_g = 1$ km intervals.
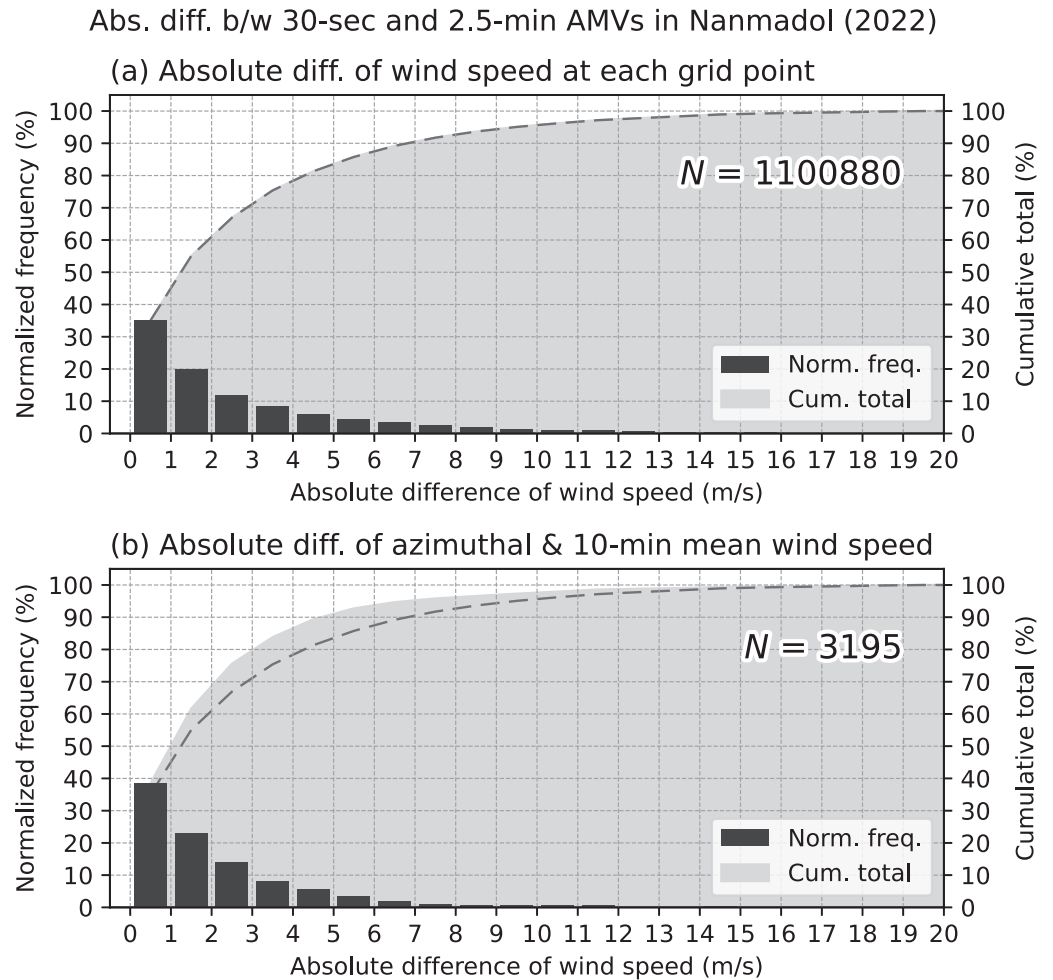
5.2. Time Evolution of the Vorticity Anomaly in Typhoon Lan

In the beginning of the analysis period of Typhoon Lan (2017), the azimuthal-mean angular velocity within a radius of 20 km was approximately half the magnitude of the angular velocity inside the inner edge of the eyewall (Figure 19a). Within the 20-km radius, the angular velocity initially increased over 00:00–01:00 UTC but then reverted back to its original value. Around 03:00 UTC, a rapid increase in angular velocity occurred, and it remained approximately 1.5 times higher than the previous value thereafter.

TH20 conducted a subjective analysis of the mesovortices in the eye of Lan by visually inspecting the visible images. These images were rotated clockwise to offset the mean low-level rotation in the eye. The use of the counter-rotated images facilitated the identification and tracking of the clouds around mesovortices. By

Figure 8. As in Figure 4, but for Typhoon Nanmadol (2022).

Abs. diff. b/w 30-sec and 2.5-min AMVs in Nanmadol (2022)

(a) Absolute diff. of wind speed at each grid point

(b) Absolute diff. of azimuthal & 10-min mean wind speed

Figure 9. As in Figure 5, but for Typhoon Nanmadol (2022).

comparing the duration of their subjectively analyzed mesovortices (Figure 19m), it is suggested that the mesovortex-1 was involved before the increase in angular velocity around 00:00–01:00 UTC, and mesovortices 2–7 were involved in the increase in angular velocity around 02:30–03:30 UTC.

These observational facts suggest a connection between increased eye rotation and horizontal mixing caused by mesovortices, as demonstrated in KE01. From Stokes' theorem, an increase in azimuthal-mean tangential velocity at a certain radius corresponds mathematically to an increase in average vorticity in the region inside that radius. Therefore, examining the time evolution of the vorticity field in the eye is one useful way to examine the cause of the rapid increase in angular velocity.

Using the AMVs derived at 1-km intervals, we focus on the distribution of vorticity anomalies with a relatively larger horizontal scale. In this study, similar to TH20, the images in the sequence were first rotated clockwise at a constant angular velocity of 1.0×10^{-3} rad/s to offset the representative low-level rotation (online supplemental Movie S1). Similarly, the same rotational component was subtracted from the AMVs. Subsequently, the resulting AMVs were smoothed using a Gaussian kernel of 10 km $\times$ 10 km (with the standard deviation of 1.67 km) and their vorticities were computed as the anomalies from the corresponding background vorticity of 2.0×10^{-3} s^{-1}. The vorticities computed on the counter-rotating coordinates represent the vorticity anomaly from the background vorticity associated with the constant angular velocity used for the counter-rotation.

Table 7
As in Table 6, but for Typhoon Nanmadol (2022)

	Tangential velocity				Radial velocity			
	(a)	(b)	(c)	(d)	(a)	(b)	(c)	(d)
cc	0.92	0.94	0.92	0.94	0.88	0.76	0.91	0.76
Bias (m/s)	−0.3	−0.3	−0.6	−0.6	0.2	0.2	0.3	0.3
RMSD (m/s)	5.4	4.4	5.4	4.4	2.2	1.2	1.7	1.0
MAD (m/s)	3.3	2.5	3.1	2.4	1.5	0.8	1.2	0.6
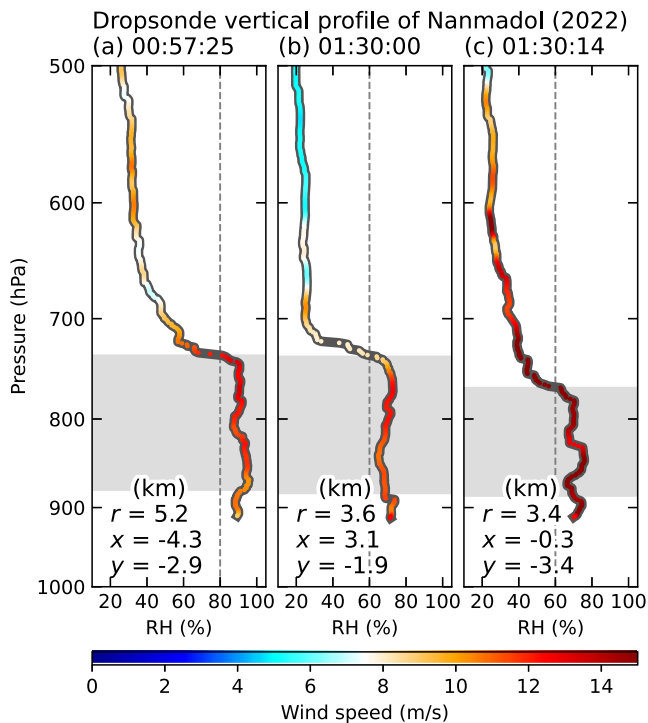
Figure 10. Vertical profiles of relative humidity and wind speed observed by GPS dropsondes compared with valid AMVs below a cloud-top height of 5 km in the eye of Typhoon Nanmadol (2022) at (a) 00:57:25, (b) 01:30:00 and (c) 01:30:14 UTC 17 September 2022. The vertical axis represents the pressure (hPa), while the horizontal axis represents the relative humidity (%). The thick curve indicates the relative humidity (%) while the color indicates wind speed (m/s). The gray shading indicates the pressure range corresponding the first 80% of the observing period from the top of the boundary layer to the surface. The boundary layer top was determined based on where the relative humidity first exceeds 80% (or 60% if the former was not reached) under 700 hPa; the threshold of relative humidity is indicated by the vertical broken line. The average time (UTC) and position (radius, x, and y; km) for the gray-shaded range are written in the panel title and lower-left corner, respectively.

The online supplemental Movie S2 shows the time evolution of vorticity anomaly field in the eye of Lan throughout the entire analysis period. Within a 20-km radius, during the first half of the analysis period (Figures 20a–20e), there was a concentration of negative vorticity anomalies that occupied about half of the circular area. In contrast, in the latter half (Figures 20e–20i), the area occupied by these negative anomalies decreased, and positive vorticity anomalies became dominant. This corresponds to the fact that the azimuthally-averaged angular velocities (or tangential velocities) around the 20-km radius (Figure 19a) were faster in the latter half of the analysis period than in the first half.

Next, our focus shifts to the distribution of vorticity anomalies during the temporary increase in angular velocity at 00:00–01:00 UTC (Figure 19a) within a 20-km radius. At 23:44 UTC (Figure 21a), negative anomalies were dominant within a radius of 20 km. At 23:57 UTC (Figure 21b), the mesovortex-1 appeared from the eastern side (upper-right quadrant in the panel). The surrounding positive vorticity anomaly gradually shifted inward, occupying half of the 20-km radius circle by 00:59 UTC (Figures 21c–21g). After that, the positive vorticity anomaly shifted outward, and the storm center again became dominated by negative vorticity anomaly (Figures 21f–21i). Since the positive vorticity anomaly area were moved inward with mesovortex-1 (Figure 21), the subsequent increase in angular velocity in the eye may have been induced by the mesovortex. Subsequently, as the negative vorticity anomaly returned to the storm center, the angular velocities within the 20-km radius reverted back to their original values.

We then shift our focus to the vorticity anomaly distribution during the rapid increase in angular velocity, observed around 02:30–03:30 UTC. At 02:22 UTC (Figure 22a), negative anomalies associated with mesovortex-6 were located inside the 20-km radius, while the positive anomalies associated with mesovortex-5 were located southwestern side (upper-left quadrant in the panel) around the 20-km radius. Subsequently, the positive vorticity anomalies shifted inward and the negative vorticity shifted outward (Figures 22b–22d), and by 03:12 UTC (Figures 22e and 22f), a portion of the negative vorticity anomaly had moved outside the 20-km radius. After 03:22 UTC (Figures 22g–22i), the negative anomaly weakened slightly and

decreased in size. At this point, positive vorticity anomalies became dominant within the 20-km radius. From the time evolution of the vorticity anomalies, it is hypothesized that the mesovortices played a role in the increase in angular velocity within the radius of 20 km around 02:30–03:30 UTC. In the subsequent subsection, the hypothesis is explored by examining the fluctuations in angular momentum and horizontal eddy forcing.

In Figures 20–22, the overlay of vorticity anomaly field and visible imagery generally shows a correspondence between the regions of negative vorticity anomaly and the areas with fewer clouds (although not necessarily cloud-free), and vice versa. The relationship between vorticity anomaly and cloud distribution is likely related to mixing processes between eyewall-originated moist air and eye-originated dry air, but further examination is needed in future work.

5.3. Angular Momentum Variation and Horizontal Eddy Forcing

In the previous section, it was hypothesized that the rapid increase in angular velocity in the eye of Typhoon Lan was due to the angular momentum transport associated with the mesovortices. In this section, we further examine it in terms of the variations in angular momentum and horizontal eddy forcing. As described in H23, the following equation can be derived from the azimuthal component of the momentum equation:
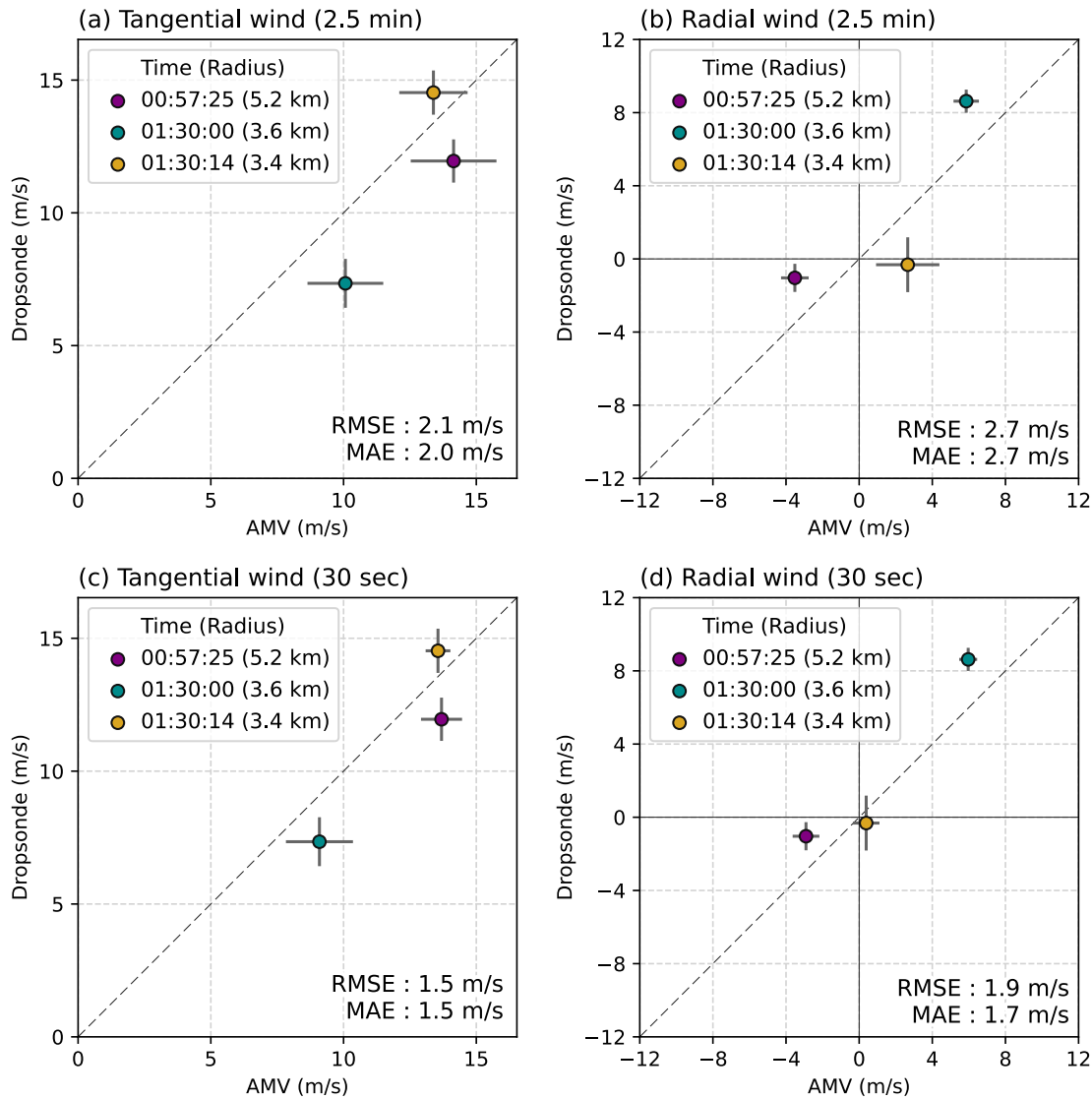
Figure 11. Comparison of (left) tangential and (right) radial velocities from dropsondes and AMVs in the eye of Typhoon Nanmadol (2022) obtained from (upper) 2.5-min and (lower) 30-s interval image sequences. The wind speed of the dropsonde was obtained by averaging over the boundary layer except near surface (gray-shaded range in Figure 10). The error bar for the dropsonde represents the standard deviation of the wind speeds within that range. The reference time and radius of the dropsonde, obtained by averaging over that range, are listed in the upper-left corner. The AMV used for the comparison was obtained by linear interpolation at the reference time and position of the dropsonde after applying a spatial running mean using a 4 km × 4 km Gaussian kernel (standard deviation of 0.67 km). The error bar for the AMV represents the standard deviation of wind speeds of AMVs at eight points on the time-space grid that encloses the reference time and position of the dropsonde. The root-mean-square error (RMSE) and the mean-absolute error (MAE) are written in the lower-right corner in each panel.

$$\frac{\mathrm{d}}{\mathrm{d}t} \int_0^R r\overline{m}\,\mathrm{d}r = -R\overline{mu} - \int_0^R r\frac{\partial(\overline{mw})}{\partial z}\mathrm{d}r + \int_0^R r\overline{X}\mathrm{d}r \tag{1}$$

where t is time, r is radius, m is the absolute angular momentum per unit mass $[m = rv + (fr^2/2)$, v is tangential velocity, and f is the Coriolis parameter], overline represents the azimuthal mean, z is altitude, and the X is the frictional force in the momentum equation. It is worth noting that if the Coriolis term is negligible, the integrand $r\overline{m}$ is nearly proportional to $R^3\overline{\omega}$, where $\overline{\omega}$ represents the angular velocity at $r = R$. Consequently, the radially
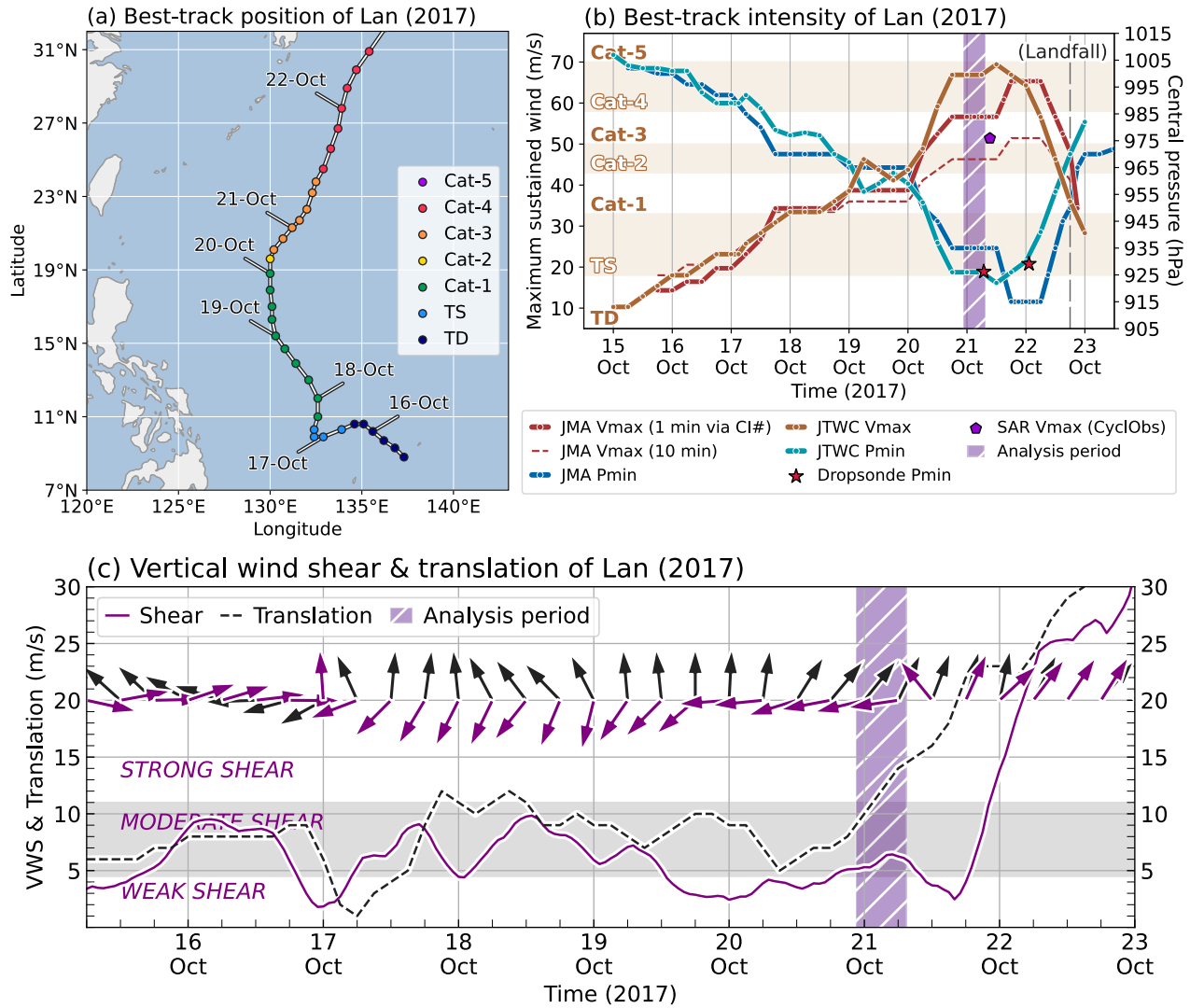
Figure 12. As in Figure 2, but for Typhoon Lan (2017). The red star indicates the central pressure obtained from the T-PARCII dropsonde observation.

integrated angular momentum over the radius from 0 to R, denoted as $M(R) \equiv \int_0^R r\overline{m}\,dr$, is dominated by the rotation at around $r = R$.

The 10-min running-mean radially integrated angular momentum $M(R)$ up to $R = 18$ km (Figure 23a) undergoes a significant change in magnitude before and after the rapid acceleration that occurred between 02:30 and 03:30 UTC 21 October (purple shaded period), as can be observed from Figure 19a. During this period, the time derivative of $M(R)$ (black curve in Figure 23b) is predominantly explained by the horizontal wavenumber-1 forcing (red curve). The time-averaged profiles of both variables as functions of the radius between 02:30 and 03:30 UTC (Figure 23c) show positive values and similar magnitudes, particularly in the radial range of 13–18 km. Therefore, this observation is insensitive to the choice of R around that range. This suggests that the acceleration of low-level rotation in the eye over 02:30–03:30 UTC can be attributed to the wavenumber-1 horizontal angular momentum transport, rather than wavenumber-0 or wavenumber higher than or equal to 2. Note that the quantification of the second and third terms on the right-hand side of Equation 1 has not been conducted. Therefore, the observed quantitative agreement in Figure 23 might be coincidental. However, one can say that the angular momentum transport by the wavenumber-1 component is qualitatively capable of causing observed speed-up.
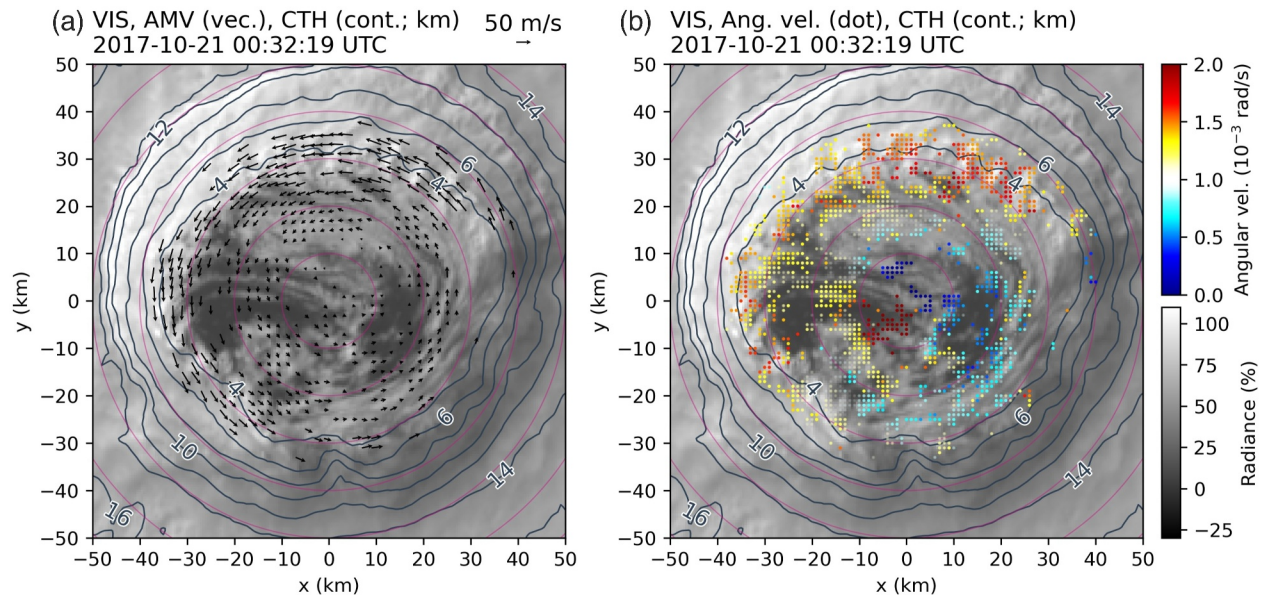
Figure 13. (a) As in Figure 3a, but for Typhoon Lan (2017) at 00:32:19 UTC 21 October 2017. The AMVs were derived at $H_g = 1$ km intervals, but they are plotted at 2 km intervals for visualization. (b) Angular velocities (color dots) of AMVs but visualized at 1 km intervals.

In the linear theory of barotropic instability (Schubert et al., 1999), it is known that mesovortices form after exponentially growing wave with wavenumbers higher than or equal to 2 breaks down. During the nonlinear regime, these mesovortices merge through horizontal mixing, resulting in a monopole-like vorticity distribution. In this process, the low vorticity region near the center of the storm is ejected outward, at which time the vorticity distribution becomes wavenumber-1 like (Figure 3 in Schubert et al., 1999, Figure 7 in Hendricks et al., 2009).

Our analysis has shown that the increase in angular momentum in the eye of the storm between 02:30 and 03:30 UTC was primarily driven by wavenumber-1 forcing, indicating that the system had already entered the nonlinear regime. The temporal evolution of the vorticity field (Figure 22) also supports the idea of low vorticity regions being expelled with azimuthal wavenumber-1 characteristics. Therefore, we suggest that the ejection of the low vorticity region near the center during the nonlinear regime explains the rapid acceleration in angular velocity in the eye of Lan. The potential importance of this process was previously speculated by H23, and our study provides observational support for it.

While the rapid acceleration of rotation in the eye of Lan did occur and may be related to mesovortices, it should not be considered a "regime transition" as defined by KE01. The term was introduced to describe the shift from the first regime, characterized by higher angular velocity in the eyewall and relatively lower values in the eye, to the second regime, characterized by nearly monotonic radial profiles of angular velocity with the highest values concentrated near the center of the eye. If the rapid acceleration around 03:00 UTC is considered a "regime transition," then the dynamic and thermodynamic structure around 06:00 UTC, where the dropsonde observations were conducted, should exhibit characteristics of regime 2. However, as shown in Yamada et al. (2021), such regime-2 like structure was not diagnosed. Note that the transition cannot be diagnosed based solely on AMVs because they do not provide the low-level wind distribution in the eyewall region. Another factor to consider is the process of alternating transitions between regime 1 and regime 2, known as the "inner-core vacillation cycle," which has been investigated in numerical simulations (Hankinson et al., 2014; Hardy et al., 2021; Nguyen et al., 2011; Reif et al., 2014). However, in the eye of Lan, there were no apparent alterations in the shape of the radial profile of the angular velocity within the eye following the rapid increase in angular velocity (Figure 19a).

6. Conclusions

Observations of wind distribution in the eye of TCs are still limited. In a recent study, the high-resolution AMVs in the eye were successfully derived from research-based 30-s special observations conducted with *Himawari-8* satellite (H23). However, steady 30-s observations are not yet available for operational use. In this study, we
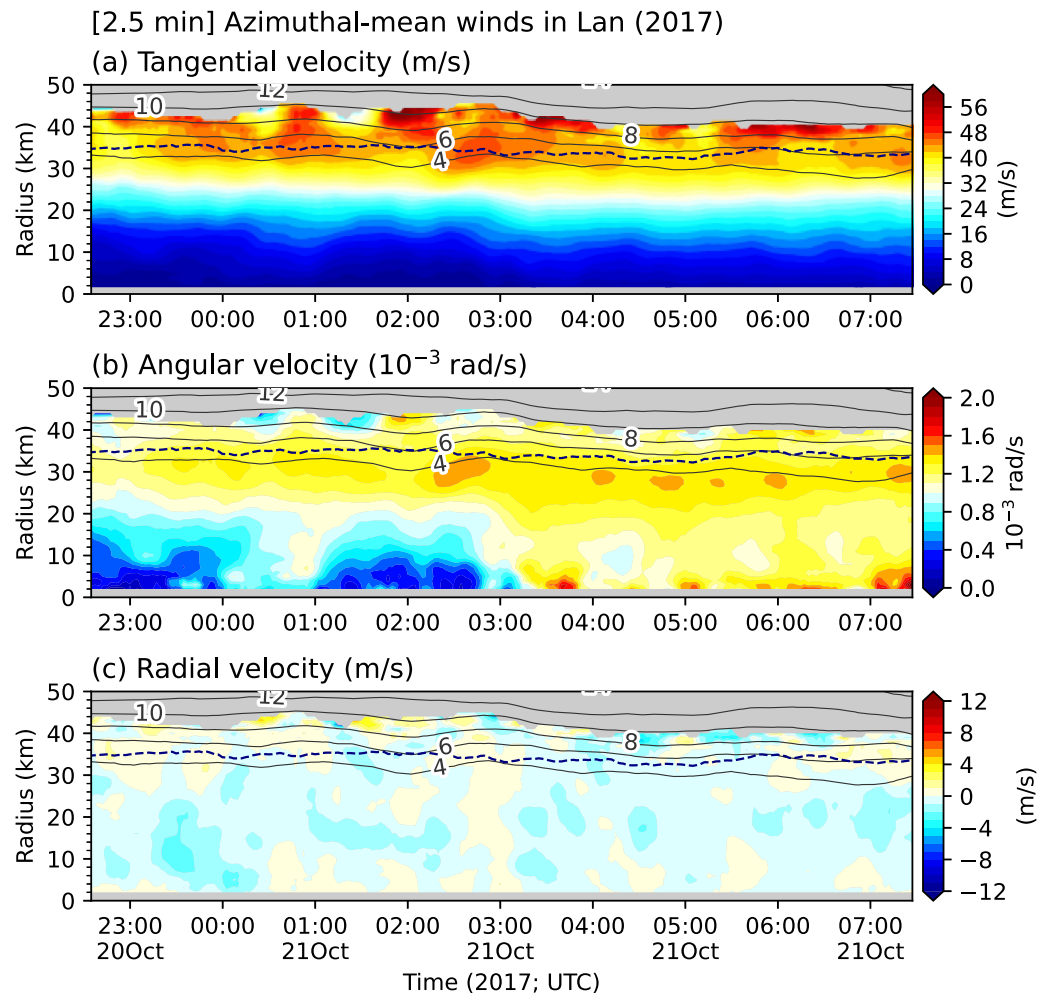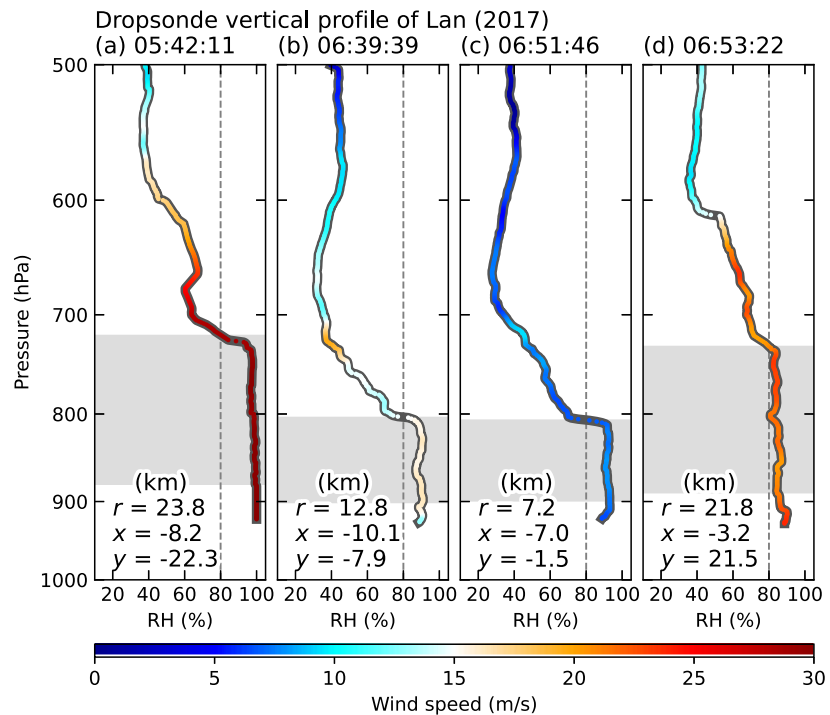
Figure 14. As in Figures 4a–4c, but for Typhoon Lan (2017).

extended the method of H23 to develop a new method for deriving AMVs from operational observations, including relatively longer time intervals such as 2.5-min interval of the *Himawari-8*. The developed method is designed specifically for TCs and considers their rotation. It involves selecting the appropriate rotation speed from multiple local rotation speeds by considering continuity among neighboring grid points. Additionally, a special approach was made for tracking the striations, which are characteristic features found in intense TCs. Considering the characteristics of TCs has enabled the estimation of motions not captured by the method of H23. However, increasing parameters through method extension introduces the drawback of heightened subjectivity. Therefore, users may need to try various settings to evaluate the robustness of the results.

The method was applied to 2.5-min interval image sequences of three TCs, Lan (2017), Haishen (2020), and Nanmadol (2022), observed by the *Himawari-8* satellite. The obtained AMVs were compared with AMVs derived from the research-based 30-s *Himawari-8* special observations conducted for Haishen and Nanmadol. In the eye of Haishen (Nanmadol), more than 60% (55%) of the AMVs had absolute wind speed differences within 2 m/s. In both cases, the azimuthal averaging significantly decreased the differences. The obtained AMVs were also compared with the in-situ observations using dropsondes conducted for Lan and Nanmadol. The AMVs obtained from the 2.5-min interval images in the eye were in good agreement with the dropsonde observations: in the eye of Nanmadol (Lan), the RMSE was 2.1 (1.7) m/s for tangential velocity and 2.7 (1.1) m/s for radial velocity. It should be noted that the small number of samples used for comparison may include sampling errors.

Asymmetric motions of the AMVs obtained in the eye revealed the transient azimuthal wavenumber-1 features in all three TCs. These features were consistent with the algebraically growing wavenumber-1 disturbances. In the
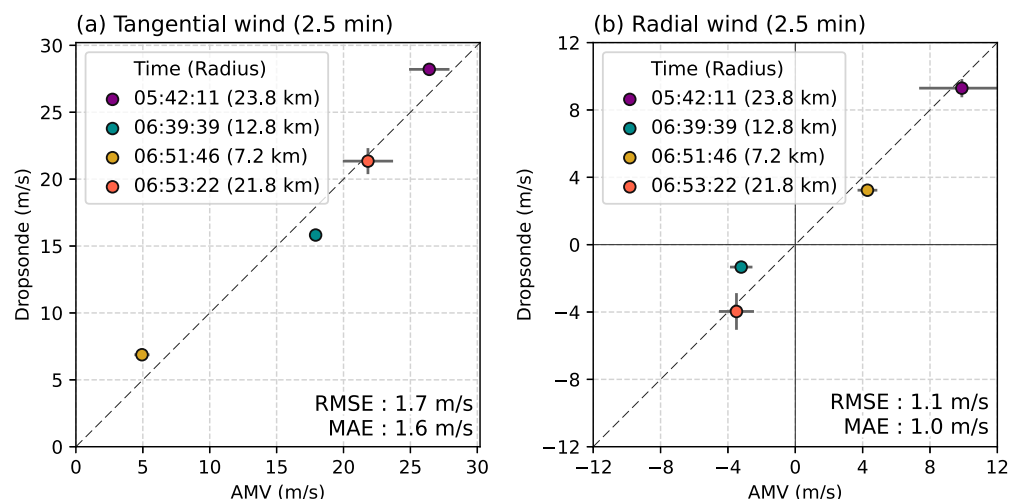
Figure 15. As in Figure 10, but for Typhoon Lan (2017) at (a) 0542:11, (b) 0639:39, (c) 0651:46, and (d) 06:53:22 UTC 21 October 2017.

eye of Lan, the angular velocity in the eye increased by ∼1.5 times within 1 hr. This short-term increase was further examined. Visualization of low-level vorticity in the eye and angular momentum budget analysis suggested that angular momentum transport associated with mesovortices had played an important role in the increase of tangential wind and the homogenization of angular velocity in the eye of Lan.

The results presented in this study highlight the significant potential of utilizing operational rapid-scan observations from the latest GMSs to investigate the dynamics of TCs. Future work would involve a statistical study applying the developed method to a larger number of TC cases. It is also interesting to explore the relationship


Figure 16. As in Figures 11a and 11b, but for Typhoon Lan (2017). The reference time, position, and wind speed of the dropsondes are obtained by averaging over the gray-shaded range in Figure 15.
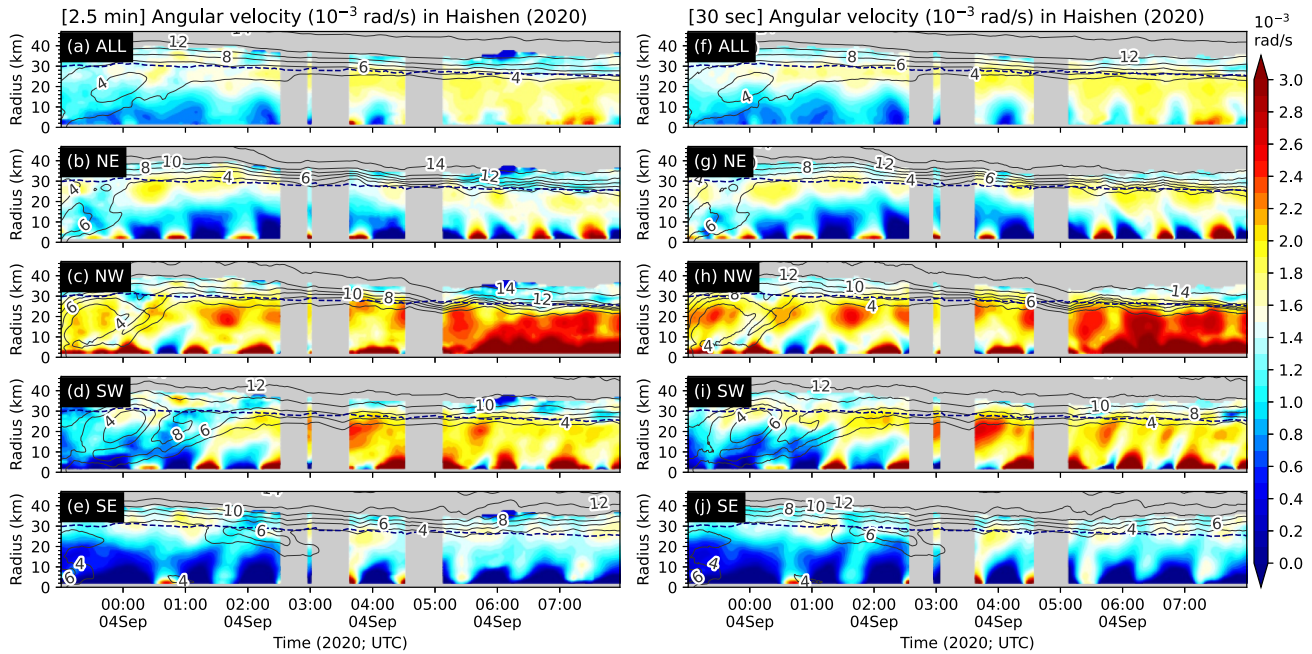
Figure 17. Azimuthal-mean and 10-min running-mean angular velocity in the eye of Typhoon Haishen (2020) obtained from (left) 2.5-min and (right) 30-s interval image sequences computed in (a),(f) all azimuths, (b),(g) northeast quadrant, (c),(h) northwest quadrant, (d),(i) southwest quadrant, and (e),(j) southeast quadrant, respectively. The black contours represent the cloud-top height (km) with corresponding azimuthal averaging. The blue dashed contour indicates the sea-surface (10-m altitude) RMWs estimated from the GMS-measured eye radius when the storm has a clear eye, using the method proposed by Tsukada and Horinouchi (2023).

between asymmetry in the eye and eyewall lightning activity (Duran et al., 2021). Additionally, combining low-level AMVs in the eye and the Doppler velocity in the eyewall observed from radar has the potential to provide new insights into the long-term behavior of the low-level dynamics of TCs.
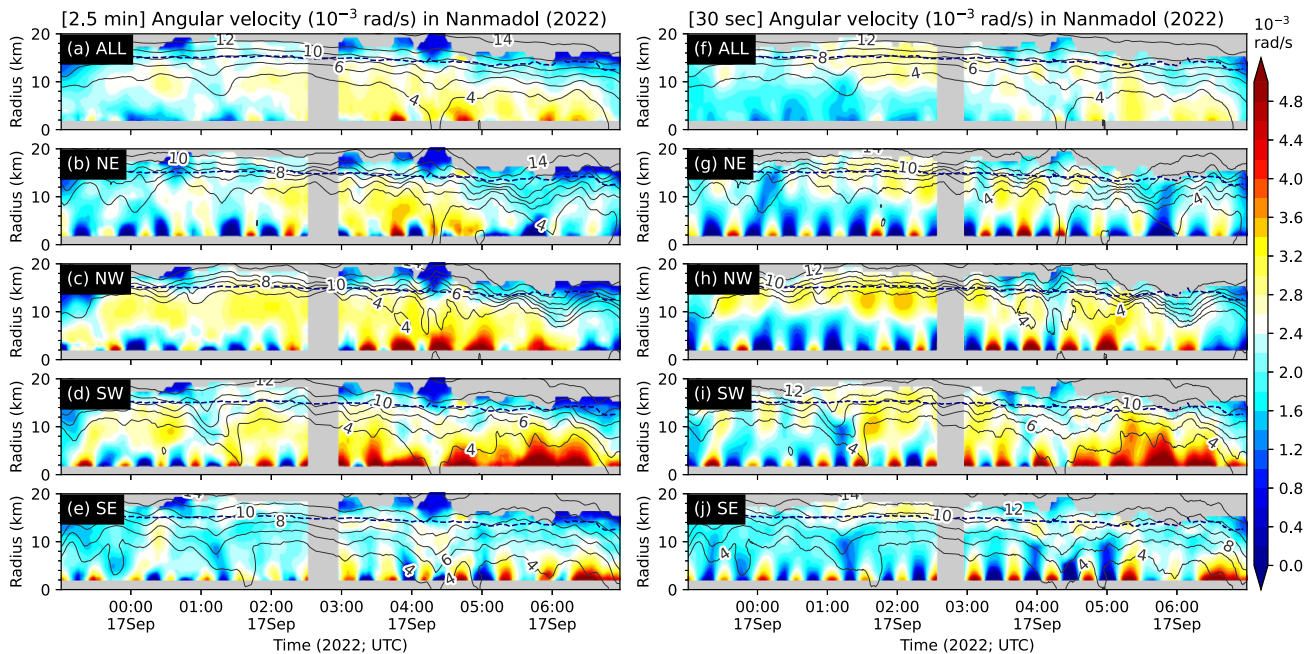

Figure 18. As in Figure 17, but for Typhoon Nanmadol (2022).
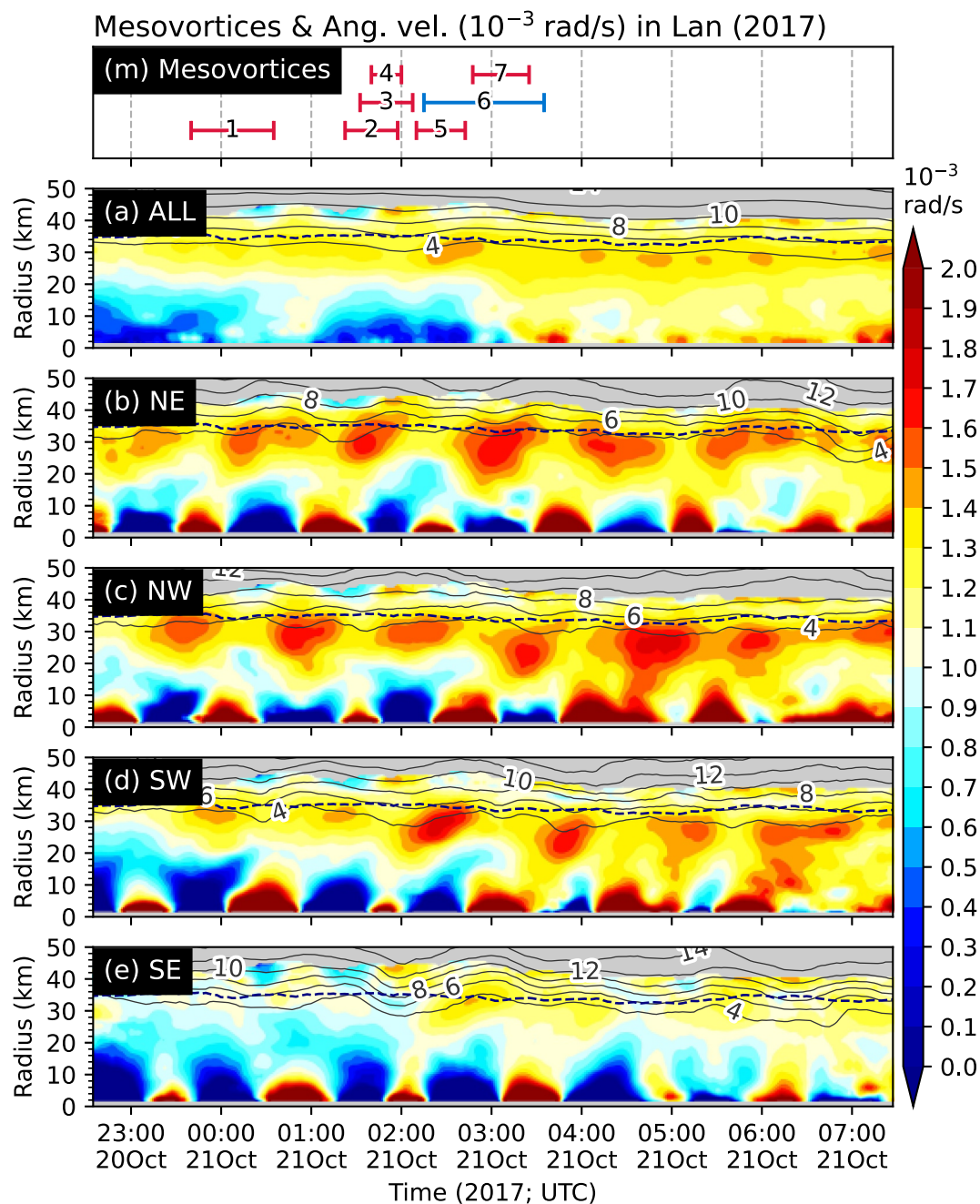
Figure 19. (a)–(e) As in Figures 17a–17e, but for Typhoon Lan (2017). (m) The red and blue bars in the top panel show the durations when the seven mesovortices, labeled with their respective IDs, were subjectively analyzed in TH20. The color of the bar indicates the sign of vorticity anomaly, with red (blue) representing positive (negative) anomaly from the twice the azimuthal-mean angular velocity at 15-km radius obtained by TH20.
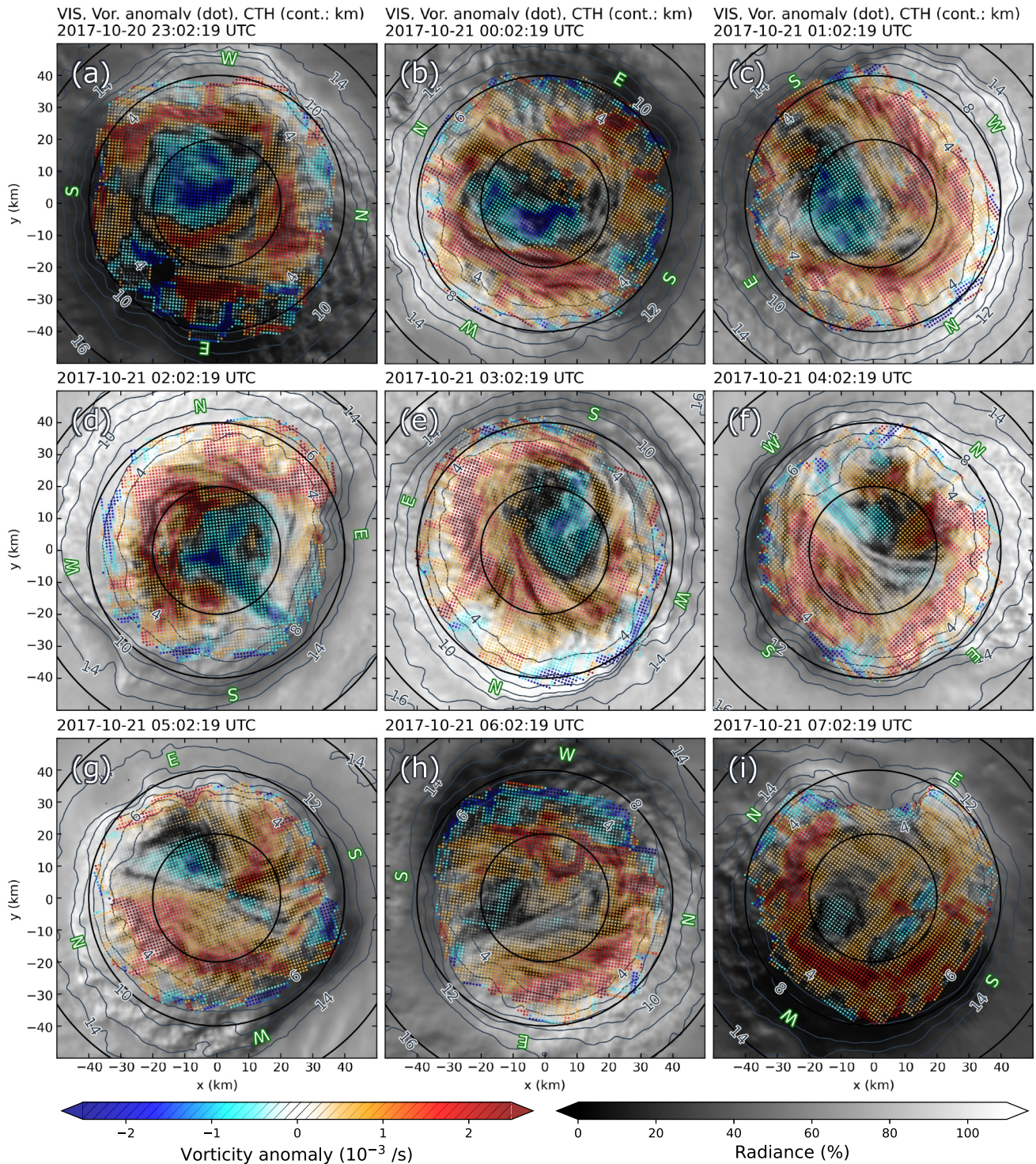
Figure 20. Vorticity anomaly (color dot) overlaid on the visible reflectivity (gray shading) in Typhoon Lan (2017) with the clockwise rotation of 1.0×10^{-3} rad/s shown every 1 hr during 8 hr over 23:02:19–07:02:19 UTC 20–21 October 2017. After subtracting the same rotational component from the AMVs, they were smoothed using a Gaussian kernel (10 km × 10 km, standard deviation of 1.67 km) and computed the vorticity anomaly from the corresponding background vorticity of 2.0×10^{-3} s^{-1}. The dot colors are translucent, and they become transparent near zero; the hatch on the color bar is drawn to indicate the transparency. The contours represent the cloud-top height (km). The bold black circles are drawn at intervals of 20-km radius. The green texts indicate the north (N), east (E), west (W), and south (S), respectively. A movie showing the time series for the entire period is available in the online supplemental Movie S2.
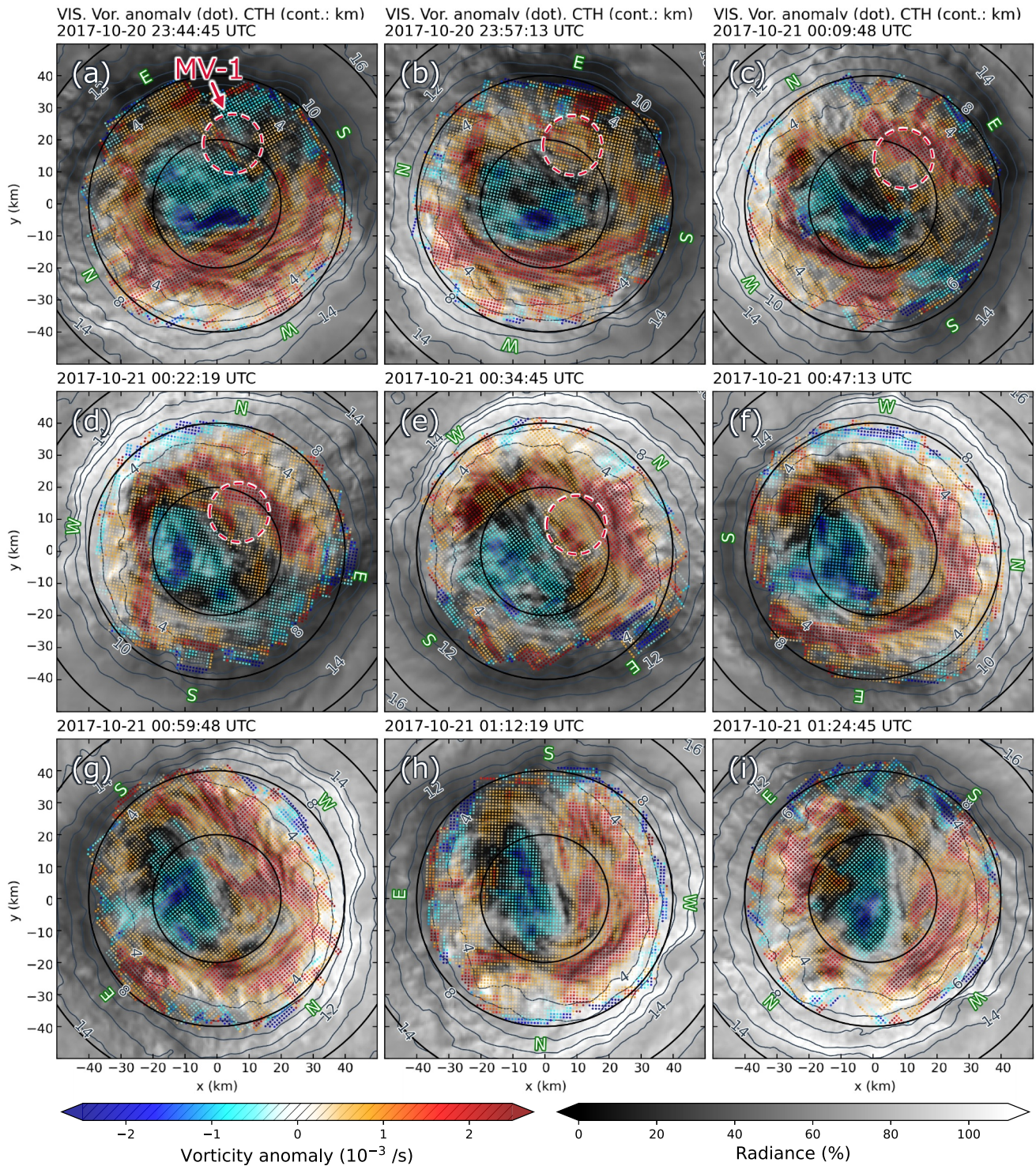
Figure 21. As in Figure 20, but shown every 12.5 min during 100 min over 23:44:45–01:24:45 UTC 20–21 October 2017. The red text and circle indicate the mesovortex and its ID with a positive vorticity anomaly, which is subjectively identified in TH20 through visual inspection of visible imagery such as Movie S1.
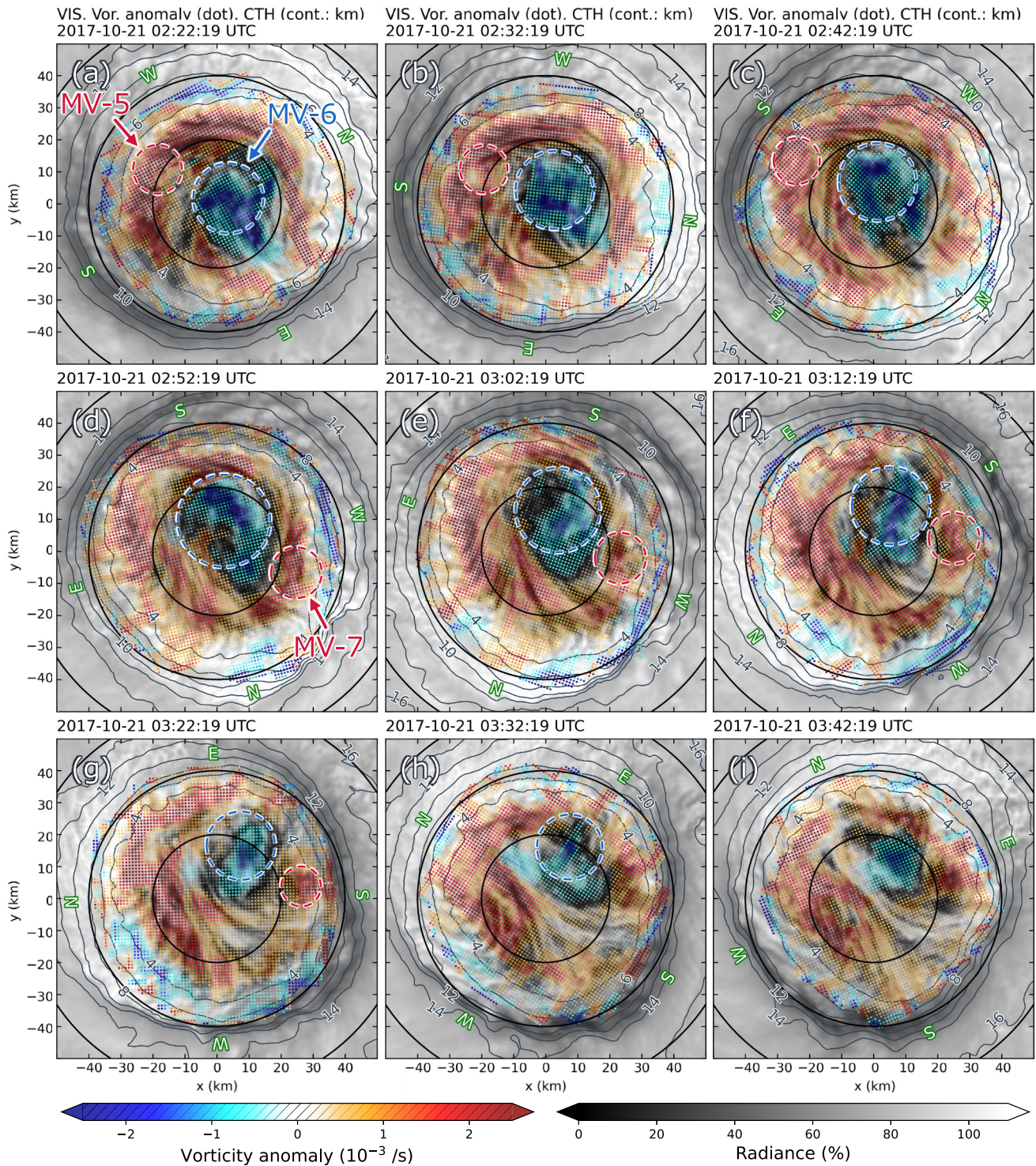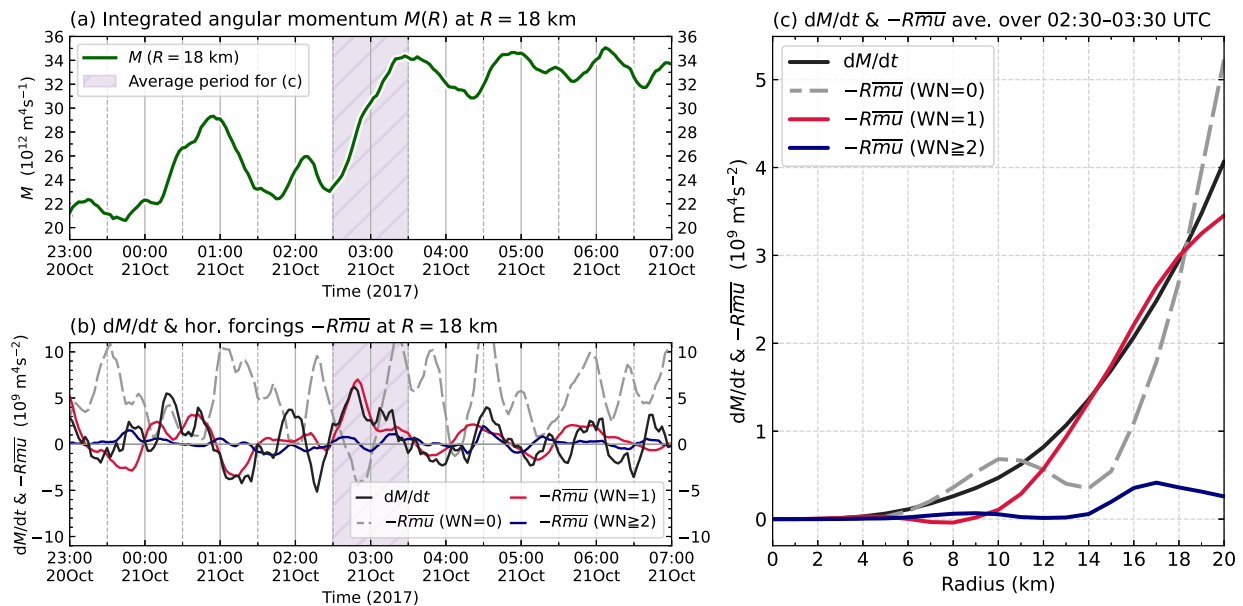
Figure 22. As in Figure 20, but shown every 10 min during 80 min over 02:22:19–03:42:19 UTC 21 October 2017. The red (blue) text and circle indicate the mesovortex and its ID with a positive (negative) vorticity anomaly, which is subjectively identified in TH20 through visual inspection of visible imagery such as Movie S1.

Figure 23. Time evolutions of (a) 10-min running-mean radially integrated angular momentum $M(R)$ up to $R = 18$ km and (b) its tendency $(d/dt)M(R)$ (derived after applying the 10-min running mean; black) and 10-min running-mean horizontal forcings $-R\overline{mu}$ associated with the wavenumber-0 (gray), wavenumber-1 (red) components, and the sum of wavenumbers higher than and equal to 2 (blue) obtained in the eye of Typhoon Lan (2017). (c) As in (b), but averaged over 02:30–03:30 UTC 21 October 2017 [indicated by the purple shaded period in (a) and (b)], shown as functions of the radius. To produce this figure, we first spatially smoothed the AMVs using a 4 km × 4 km Gaussian kernel with a standard deviation of 0.67 km. Then, we resampled the AMVs to polar coordinates and linearly interpolated any missing data along the azimuthal axis. Finally, we performed azimuthal wavenumber decomposition and averaging.

Data Availability Statement

The *Himawari-8* satellite data are publicly available at the DIAS (https://diasjp.net/en/service/himawari8-data-download/). The manually tracked storm positions, the derived atmospheric motion vectors, and the dropsonde sounding data used for comparison are available from https://doi.org/10.5281/zenodo.10798896 (Tsukada et al., 2024). The IBTrACS dataset is archived by the National Centers for Environmental Information and is available online (https://doi.org/10.25921/82ty-9e16). The ERA5 data were downloaded from Copernicus Climate Change Service (2017) (https://cds.climate.copernicus.eu/cdsapp#!/home). The sea surface wind dataset retrieved from C-band SAR satellites is available at the CyclObs (https://cyclobs.ifremer.fr/).

References

Aberson, S. D., Montgomery, M. T., Bell, M., & Black, M. (2006). Hurricane Isabel (2003): New insights into the physics of intense storms. Part II: Extreme localized wind. *Bulletin of the American Meteorological Society*, *87*(10), 1349–1354. https://doi.org/10.1175/BAMS-87-10-1349

Bessho, K., Date, K., Hayashi, M., Ikeda, A., Imai, T., Inoue, H., et al. (2016). An introduction to Himawari-8/9 — Japan's new-generation geostationary meteorological satellites. *Journal of the Meteorological Society of Japan. Ser. II*, *94*(2), 151–183. https://doi.org/10.2151/jmsj.2016-009

Bieliński, T. (2020). A parallax shift effect correction based on cloud height for geostationary satellites and radar observations. *Remote Sensing*, *12*(3), 365. https://doi.org/10.3390/rs12030365

Bluestein, H. B., & Marks, F. D. (1987). On the structure of the eyewall of Hurricane Diana (1984): Comparison of radar and visual characteristics. *Monthly Weather Review*, *115*(10), 2542–2552. https://doi.org/10.1175/1520-0493(1987)115<2542:OTSOTE>2.0.CO;2

Copernicus Climate Change Service (C3S). (2017). ERA5: Fifth generation of ECMWF atmospheric reanalysis of the global climate. Retrieved from https://cds.climate.copernicus.eu/cdsapp#!/home

Dai, Y., Majumdar, S. J., & Nolan, D. S. (2019). The outflow–rainband relationship induced by environmental flow around tropical cyclones. *Journal of the Atmospheric Sciences*, *76*(7), 1845–1863. https://doi.org/10.1175/JAS-D-18-0208.1

Dunion, J. P., Houston, S. H., Velden, C. S., & Powell, M. D. (2002). Application of surface-adjusted GOES low-level cloud-drift winds in the environment of Atlantic tropical cyclones. Part II: Integration into surface wind Analyses. *Monthly Weather Review*, *130*(5), 1347–1355. https://doi.org/10.1175/1520-0493(2002)130<1347:AOSAGL>2.0.CO;2

Dunion, J. P., & Velden, C. S. (2002). Application of surface-adjusted GOES low-level cloud-drift winds in the environment of Atlantic tropical cyclones. Part I: Methodology and validation. *Monthly Weather Review*, *130*(5), 1333–1346. https://doi.org/10.1175/1520-0493(2002)130<1333:AOSAGL>2.0.CO;2

Duran, P., Schultz, C. J., Bruning, E. C., Stevenson, S. N., PeQueen, D. J., Johnson, N. E., et al. (2021). The evolution of lightning flash density, flash size, and flash energy during Hurricane Dorian's (2019) intensification and weakening. *Geophysical Research Letters*, *48*(8). https://doi.org/10.1029/2020GL092067

Dvorak, V. F. (1984). Tropical cyclone intensity analysis using satellite data. *NOAA Technical Report NESDIS*, *11*. https://repository.library.noaa.gov/view/noaa/19322

Elsberry, R. L., Feldmeier, J. W., Chen, H.-J., & Velden, C. S. (2023). High temporal resolution analyses with GOES-16 atmospheric motion vectors of mesovortex rapid intensification in subtropical cyclone Henri (2021). *Weather and Forecasting*, *38*(7), 1173–1194. https://doi.org/10.1175/WAF-D-22-0148.1

Fleet, D., & Weiss, Y. (2006). *Optical flow estimation*. In *Handbook of Mathematical Models in Computer Vision* (pp. 237–257). Springer. https://doi.org/10.1007/0-387-28831-7_15

Fritz, S., & Winston, J. S. (1962). Synoptic use of radiation measurements from satellite TIROS-II. *Monthly Weather Review*, *90*(1), 1–9. https://doi.org/10.1175/1520-0493(1962)090<0001:suormf>2.0.co;2

Fukuda, K., Yasunaga, K., Oyama, R., Wada, A., Hamada, A., & Fudeyasu, H. (2020). The diurnal cycle of clouds in tropical cyclones over the Western North Pacific Basin. *SOLA*, *16*(0), 109–114. https://doi.org/10.2151/sola.2020-019

Guinn, T. A., & Schubert, W. H. (1993). Hurricane spiral bands. *Journal of the Atmospheric Sciences*, *50*(20), 3380–3403. https://doi.org/10.1175/1520-0469(1993)050<3380:HSB>2.0.CO;2

Hankinson, M. C. N., Reeder, M. J., Davidson, N. E., & Puri, K. (2014). Vacillation cycles in simulations of Hurricane Katrina. *Quarterly Journal of the Royal Meteorological Society*, *140*(683), 1878–1888. https://doi.org/10.1002/qj.2275

Hardy, S., Schwendike, J., Smith, R. K., Short, C. J., Reeder, M. J., & Birch, C. E. (2021). Fluctuations in inner-core structure during the rapid intensification of Super Typhoon Nepartak (2016). *Monthly Weather Review*, *149*(1), 221–243. https://doi.org/10.1175/MWR-D-19-0415.1

Hasler, A. F., Palaniappan, K., Kambhammetu, C., Black, P., Uhlhorn, E., & Chesters, D. (1998). High-resolution wind fields within the inner core and eye of a mature tropical cyclone from GOES 1-min images. *Bulletin of the American Meteorological Society*, *79*(11), 2483–2496. https://doi.org/10.1175/1520-0477(1998)079<2483:HRWFWT>2.0.CO;2

Hendricks, E. A., McNoldy, B. D., & Schubert, W. H. (2012). Observed inner-core structural variability in Hurricane Dolly (2008). *Monthly Weather Review*, *140*(12), 4066–4077. https://doi.org/10.1175/MWR-D-12-00018.1

Hendricks, E. A., & Schubert, W. H. (2010). Adiabatic rearrangement of Hollow PV Towers. *Journal of Advances in Modeling Earth Systems*, *2*(4), 19. https://doi.org/10.3894/JAMES.2010.2.8

Hendricks, E. A., Schubert, W. H., Chen, Y.-H., Kuo, H.-C., & Peng, M. S. (2014). Hurricane eyewall evolution in a forced shallow-water model. *Journal of the Atmospheric Sciences*, *71*(5), 1623–1643. https://doi.org/10.1175/JAS-D-13-0303.1

Hendricks, E. A., Schubert, W. H., Taft, R. K., Wang, H., & Kossin, J. P. (2009). Life cycles of hurricane-like vorticity rings. *Journal of the Atmospheric Sciences*, *66*(3), 705–722. https://doi.org/10.1175/2008JAS2820.1

Henken, C. C., Schmeits, M. J., Deneke, H., & Roebeling, R. A. (2011). Using MSG-SEVIRI cloud physical properties and weather radar observations for the detection of Cb/TCu clouds. *Journal of Applied Meteorology and Climatology*, *50*(7), 1587–1600. https://doi.org/10.1175/2011JAMC2601.1

Hersbach, H., Bell, B., Berrisford, P., Hirahara, S., Horányi, A., Muñoz-Sabater, J., et al. (2020). The ERA5 global reanalysis. *Quarterly Journal of the Royal Meteorological Society*, *146*(730), 1999–2049. https://doi.org/10.1002/qj.3803

Hirano, S., Ito, K., Yamada, H., Tsujino, S., Tsuboki, K., & Wu, C.-C. (2022). Deep eye clouds in Tropical Cyclone Trami (2018) during T-PARCII dropsonde observations. *Journal of the Atmospheric Sciences*, *79*(3), 683–703. https://doi.org/10.1175/JAS-D-21-0192.1

Horinouchi, T., Murakami, S., Kouyama, T., Ogohara, K., Yamazaki, A., Yamada, M., & Watanabe, S. (2017). Image velocimetry for clouds with relaxation labeling based on deformation consistency. *Measurement Science and Technology*, *28*(8), 085301. https://doi.org/10.1088/1361-6501/aa695c

Horinouchi, T., Shimada, U., & Wada, A. (2020). Convective bursts with gravity waves in tropical cyclones: Case study with the Himawari-8 satellite and idealized numerical study. *Geophysical Research Letters*, *47*(3). https://doi.org/10.1029/2019GL086295

Horinouchi, T., Tsujino, S., Hayashi, M., Shimada, U., Yanase, W., Wada, A., & Yamada, H. (2023). Stationary and transient asymmetric features in tropical cyclone eye with wavenumber-1 instability: Case study for Typhoon Haishen (2020) with atmospheric motion vectors from 30-second imaging. *Monthly Weather Review*, *151*(1), 253–273. https://doi.org/10.1175/MWR-D-22-0179.1

Inoue, T. (1987). A cloud type classification with NOAA 7 split-window measurements. *Journal of Geophysical Research: Atmospheres*, *92*(D4), 3991–4000. https://doi.org/10.1029/JD092iD04p03991

Ito, K., Yamada, H., Yamaguchi, M., Nakazawa, T., Nagahama, N., Shimizu, K., et al. (2018). Analysis and forecast using dropsonde data from the inner-core region of Tropical Cyclone Lan (2017) obtained during the first aircraft missions of T-PARCII. *SOLA*, *14*(0), 105–110. https://doi.org/10.2151/sola.2018-018

Knapp, K. R., Diamond, H. J., Kossin, J. P., Kruk, M. C., & Schreck, C. J. I. (2018). International Best Track Archive for Climate Stewardship (IBTrACS) Project, Version 4. https://doi.org/10.25921/82ty-9e16

Knapp, K. R., Kruk, M. C., Levinson, D. H., Diamond, H. J., & Neumann, C. J. (2010). The International Best Track Archive for Climate Stewardship (IBTrACS): Unifying tropical cyclone data. *Bulletin of the American Meteorological Society*, *91*(3), 363–376. https://doi.org/10.1175/2009BAMS2755.1

Koba, H., Hagiwara, T., Osano, S., & Akashi, S. (1990). Relationship between the CI-number and central pressure and maximum wind speed in typhoons [in Japanese]. *Journal of Meteorological Research*, *42*, 59–67.

Kossin, J. P., & Eastin, M. D. (2001). Two distinct regimes in the kinematic and thermodynamic structure of the hurricane eye and eyewall. *Journal of the Atmospheric Sciences*, *58*(9), 1079–1090. https://doi.org/10.1175/1520-0469(2001)058<1079:TDRITK>2.0.CO;2

Kossin, J. P., McNoldy, B. D., & Schubert, W. H. (2002). Vortical swirls in hurricane eye clouds. *Monthly Weather Review*, *130*(12), 3144–3149. https://doi.org/10.1175/1520-0493(2002)130<3144:VSIHEC>2.0.CO;2

Kossin, J. P., & Schubert, W. H. (2001). Mesovortices, polygonal flow patterns, and rapid pressure falls in hurricane-like vortices. *Journal of the Atmospheric Sciences*, *58*(15), 2196–2209. https://doi.org/10.1175/1520-0469(2001)058<2196:MPFPAR>2.0.CO;2

Kossin, J. P., & Schubert, W. H. (2004). Mesovortices in Hurricane Isabel. *Bulletin of the American Meteorological Society*, *85*(2), 151–153. https://doi.org/10.1175/BAMS-85-2-151

Lewis, B. M., & Hawkins, H. F. (1982). Polygonal eye walls and rainbands in hurricanes. *Bulletin of the American Meteorological Society*, *63*(11), 1294–1300. https://doi.org/10.1175/1520-0477(1982)063<1294:PEWARI>2.0.CO;2

Marks, F. D., Black, P. G., Montgomery, M. T., & Burpee, R. W. (2008). Structure of the eye and eyewall of Hurricane Hugo (1989). *Monthly Weather Review*, *136*(4), 1237–1259. https://doi.org/10.1175/2007MWR2073.1

Martinez, J., Bell, M. M., Rogers, R. F., & Doyle, J. D. (2019). Axisymmetric potential vorticity evolution of Hurricane Patricia (2015). *Journal of the Atmospheric Sciences*, *76*(7), 2043–2063. https://doi.org/10.1175/JAS-D-18-0373.1

Mei, W., & Xie, S.-P. (2016). Intensification of landfalling typhoons over the Northwest Pacific since the late 1970s. *Nature Geoscience*, *9*(10), 753–757. https://doi.org/10.1038/ngeo2792

Menzel, W. P. (2001). Cloud tracking with satellite imagery: From the pioneering work of Ted Fujita to the present. *Bulletin of the American Meteorological Society*, *82*(1), 33–47. https://doi.org/10.1175/1520-0477(2001)082<0033:CTWSIF>2.3.CO;2

Molinari, J., & Vollaro, D. (1989). External influences on hurricane intensity. Part I: Outflow layer eddy angular momentum fluxes. *Journal of the Atmospheric Sciences*, *46*(8), 1093–1105. https://doi.org/10.1175/1520-0469(1989)046<1093:EIOHIP>2.0.CO;2

Montgomery, M. T., & Kallenbach, R. J. (1997). A theory for vortex rossby-waves and its application to spiral bands and intensity changes in hurricanes. *Quarterly Journal of the Royal Meteorological Society*, *123*(538), 435–465. https://doi.org/10.1002/qj.49712353810

Mouche, A., Chapron, B., Knaff, J., Zhao, Y., Zhang, B., & Combot, C. (2019). Copolarized and cross-polarized SAR measurements for high-resolution description of major hurricane wind structures: Application to Irma category 5 hurricane. *Journal of Geophysical Research: Oceans*, *124*(6), 3905–3922. https://doi.org/10.1029/2019JC015056

Mouche, A. A., Chapron, B., Zhang, B., & Husson, R. (2017). Combined co- and cross-polarized SAR measurements under extreme wind conditions. *IEEE Transactions on Geoscience and Remote Sensing*, *55*(12), 6746–6755. https://doi.org/10.1109/TGRS.2017.2732508

Muramatsu, T. (1986). The structure of polygonal eye of a typhoon. *Journal of the Meteorological Society of Japan. Ser. II*, *64*(6), 913–921. https://doi.org/10.2151/jmsj1965.64.6_913

Nguyen, M. C., Reeder, M. J., Davidson, N. E., Smith, R. K., & Montgomery, M. T. (2011). Inner-core vacillation cycles during the intensification of Hurricane Katrina: Inner-core vacillation during Hurricane Katrina. *Quarterly Journal of the Royal Meteorological Society*, *137*(657), 829–844. https://doi.org/10.1002/qj.823

Nolan, D. S., & Montgomery, M. T. (2000). The algebraic growth of wavenumber one disturbances in hurricane-like vortices. *Journal of the Atmospheric Sciences*, *57*(21), 3514–3538. https://doi.org/10.1175/1520-0469(2000)057<3514:TAGOWO>2.0.CO;2

Oyama, R. (2017). Relationship between tropical cyclone intensification and cloud-top outflow revealed by upper-tropospheric atmospheric motion vectors. *Journal of Applied Meteorology and Climatology*, *56*(10), 2801–2819. https://doi.org/10.1175/JAMC-D-17-0058.1

Oyama, R., Wada, A., & Sawada, M. (2016). Intensification of Typhoon Danas (1324) captured by MTSAT upper tropospheric atmospheric motion vectors. *SOLA*, *12*(0), 135–139. https://doi.org/10.2151/sola.2016-029

Raspaud, M., Hoese, D., Dybbroe, A., Lahtinen, P., Devasthale, A., Itkin, M., et al. (2018). PyTroll: An open-source, community-driven Python framework to process earth observation satellite data. *Bulletin of the American Meteorological Society*, *99*(7), 1329–1336. https://doi.org/10.1175/BAMS-D-17-0277.1

Reif, M., Reeder, M., & Hankinson, M. (2014). Vacillation cycles in WRF simulations of Hurricane Katrina. *Australian Meteorological and Oceanographic Journal*, *64*(2), 123–132. https://doi.org/10.22499/2.6402.004

Rios-Berrios, R., & Torn, R. D. (2017). Climatological analysis of tropical cyclone intensity changes under moderate vertical wind shear. *Monthly Weather Review*, *145*(5), 1717–1738. https://doi.org/10.1175/MWR-D-16-0350.1

Roebeling, R. A., & Holleman, I. (2009). SEVIRI rainfall retrieval and validation using weather radar observations. *Journal of Geophysical Research*, *114*(D21), D21202. https://doi.org/10.1029/2009JD012102

Rosenfeld, A., Hummel, R. A., & Zucker, S. W. (1976). Scene labeling by relaxation operations. *IEEE Transactions on Systems, Man, and Cybernetics*, *SMC-6*(6), 420–433. https://doi.org/10.1109/TSMC.1976.4309519

Rozoff, C. M., Kossin, J. P., Schubert, W. H., & Mulero, P. J. (2009). Internal control of hurricane intensity variability: The dual nature of potential vorticity mixing. *Journal of the Atmospheric Sciences*, *66*(1), 133–147. https://doi.org/10.1175/2008JAS2717.1

Ryglicki, D. R., Velden, C. S., Reasor, P. D., Hodyss, D., & Doyle, J. D. (2021). Observations of atypical rapid intensification characteristics in hurricane Dorian (2019). *Monthly Weather Review*, *149*(7), 2131–2150. https://doi.org/10.1175/MWR-D-20-0413.1

Schmit, T. J., Griffith, P., Gunshor, M. M., Daniels, J. M., Goodman, S. J., & Lebair, W. J. (2017). A closer look at the ABI on the GOES-R series. *Bulletin of the American Meteorological Society*, *98*(4), 681–698. https://doi.org/10.1175/BAMS-D-15-00230.1

Schubert, W. H., Montgomery, M. T., Taft, R. K., Guinn, T. A., Fulton, S. R., Kossin, J. P., & Edwards, J. P. (1999). Polygonal eyewalls, asymmetric eye contraction, and potential vorticity mixing in hurricanes. *Journal of the Atmospheric Sciences*, *56*(9), 27–1223. https://doi.org/10.1175/1520-0469(1999)056<1197:peaeca>2.0.co;2

Schultz, H. (1990). A circular median filter approach for resolving directional ambiguities in wind fields retrieved from spaceborne scatterometer data. *Journal of Geophysical Research: Oceans*, *95*(C4), 5291–5303. https://doi.org/10.1029/JC095iC04p05291

Sears, J., & Velden, C. S. (2012). Validation of satellite-derived atmospheric motion vectors and analyses around tropical disturbances. *Journal of Applied Meteorology and Climatology*, *51*(10), 1823–1834. https://doi.org/10.1175/JAMC-D-12-024.1

Simpson, R. H. (1974). The hurricane disaster—Potential scale. *Weatherwise*, *27*(4), 169–186. https://doi.org/10.1080/00431672.1974.9931702

Slocum, C. J., Razin, M. N., Knaff, J. A., & Stow, J. P. (2022). Does ERA5 mark a new era for resolving the tropical cyclone environment? *Journal of Climate*, *35*(21), 1–39. https://doi.org/10.1175/JCLI-D-22-0127.1

Smith, R. A., & Rosenbluth, M. N. (1990). Algebraic instability of hollow electron columns and cylindrical vortices. *Physical Review Letters*, *64*(6), 649–652. https://doi.org/10.1103/PhysRevLett.64.649

Stettner, D., Velden, C., Rabin, R., Wanzong, S., Daniels, J., & Bresky, W. (2019). Development of enhanced vortex-scale atmospheric motion vectors for hurricane applications. *Remote Sensing*, *11*(17), 1981. https://doi.org/10.3390/rs11171981

Tsujino, S., Horinouchi, T., Tsukada, T., Kuo, H.-C., Yamada, H., & Tsuboki, K. (2021). Inner-core wind field in a concentric eyewall replacement of Typhoon Trami (2018): A quantitative analysis based on the Himawari-8 satellite. *Journal of Geophysical Research: Atmospheres*, *126*(7). https://doi.org/10.1029/2020JD034434

Tsukada, T., & Horinouchi, T. (2020). Estimation of the tangential winds and asymmetric structures in typhoon inner core region using Himawari-8. *Geophysical Research Letters*, *47*(11). https://doi.org/10.1029/2020GL087637

Tsukada, T., & Horinouchi, T. (2023). Strong relationship between eye radius and radius of maximum wind of tropical cyclones. *Monthly Weather Review*, *151*(2), 569–588. https://doi.org/10.1175/MWR-D-22-0106.1

Tsukada, T., Horinouchi, T., & Tsujino, S. (2024). Storm positions, AMVs, and dropsonde sounding data used in Tsukada et al. (2024). [Dataset]. *Zenodo*. https://doi.org/10.5281/zenodo.10798896

Velden, C. S., Olander, T. L., & Wanzong, S. (1998). The impact of multispectral *GOES-8* wind information on Atlantic tropical cyclone track forecasts in 1995. Part I: Dataset methodology, description, and case analysis. *Monthly Weather Review*, *126*(5), 1202–1218. https://doi.org/10.1175/1520-0493(1998)126<1202:TIOMGW>2.0.CO;2

Velden, C. S., & Sears, J. (2014). Computing deep-tropospheric vertical wind shear analyses for tropical cyclone applications: Does the methodology matter? *Weather and Forecasting*, *29*(5), 1169–1180. https://doi.org/10.1175/WAF-D-13-00147.1

Vicente, G. A., Davenport, J. C., & Scofield, R. A. (2002). The role of orographic and parallax corrections on real time high resolution satellite rainfall rate distribution. *International Journal of Remote Sensing*, *23*(2), 221–230. https://doi.org/10.1080/01431160010006935

Wingo, S. M., & Knupp, K. R. (2016). Kinematic structure of mesovortices in the eyewall of Hurricane Ike (2008) derived from ground-based dual-Doppler analysis. *Monthly Weather Review*, *144*(11), 4245–4263. https://doi.org/10.1175/MWR-D-16-0085.1

Wolberg, G. (1990). *Digital image warping*. IEEE computer society press Los Alamitos.

Wurman, J., & Kosiba, K. (2018). The role of small-scale vortices in enhancing surface winds and damage in Hurricane Harvey (2017). *Monthly Weather Review*, *146*(3), 713–722. https://doi.org/10.1175/MWR-D-17-0327.1

Yamada, H., Ito, K., Tsuboki, K., Shinoda, T., Ohigashi, T., Yamaguchi, M., et al. (2021). The double warm-core structure of Typhoon Lan (2017) as observed through the first Japanese eyewall-penetrating aircraft reconnaissance. *Journal of the Meteorological Society of Japan. Ser. II*, *99*(5), 1297–1327. https://doi.org/10.2151/jmsj.2021-063

Yau, M. K., Liu, Y., Zhang, D.-L., & Chen, Y. (2004). A multiscale numerical study of Hurricane Andrew (1992). Part VI: Small-scale inner-core structures and wind streaks. *Monthly Weather Review*, *132*(6), 1410–1433. https://doi.org/10.1175/1520-0493(2004)132<1410:AMNSOH>2.0.CO;2

Zhao, Y., Mouche, A. A., Chapron, B., & Reul, N. (2018). Direct comparison between active C-band radar and passive L-band radiometer measurements: Extreme event cases. *IEEE Geoscience and Remote Sensing Letters*, *15*(6), 897–901. https://doi.org/10.1109/LGRS.2018.2811712